Development of an Equatorial Electro-Jet model based on the dense Peruvian magnetometer array

松下, 拓輝

https://doi.org/10.15017/1931715

出版情報：九州大学, 2017, 博士（理学）, 課程博士
バージョン：
権利関係：

Development of an Equatorial Electro-Jet model based on the dense Peruvian magnetometer array

A THESIS
SUBMITTED
BY
HIROKI MATSUSHITA
TO
THE DEPARTMENT OF EARTH AND PLANETARY SCIENCES
GRADUATE SCHOOL OF SCIENCE
IN PARTIAL FULFILLMENT OF THE REQUIREMENTS
FOR THE DEGREE
OF
DOCTOR OF SCIENCE
KYUSHU UNIVERSITY
FUKUOKA, JAPAN
MARCH 2018

Abstract

The equatorial electrojet (EEJ) is an eastward-flowing electric current in the equatorial region of the Earth's ionosphere. It is well known as the source of the abnormal enhancement of the daily variation during geomagnetic quiet time at the magnetic dip equator. It was reported that equatorial enhancement has been observed not only in the daily variation of the Earth's magnetic field but also in geomagnetic-disturbance phenomena such as DP2 and SSC. Therefore, the development of a model to represent such latitudinal profiles is important for space weather studies.

Although past researchers have investigated the latitudinal profile of the EEJ using the magnetic data of a Low Earth Orbit (LEO) satellite, it was difficult to investigate its time development due to the characteristics of an LEO satellite. By contrast, the magnetic data on the ground had important roles in the investigation into the time development of a phenomenon or a magnetic local time (MLT) structure since these data are fixed to a certain coordinate system and are continuously derived there. However, it was difficult to identify whether an increase or decrease in the magnetic field variation was caused by the change of current intensity or the size of the current such as the width.

The MAGnetic Data Acquisition System (MAGDAS), which was organized by the International Center for Space Weather Science and Education (ICSWSE), is the largest network of ground magnetometers in the world. MAGDAS was expanded to Peru and the dense magnetometer array in Peru was developed. As a result, we developed a model that continuously derives the latitudinal profile of the EEJ using that data. The best set of parameters for the EEJ model was determined using the method of least squares between the observed field and the calculated field from the modeled EEJ current. The EEJ model was evaluated using Swarm data, which is one of LEO satellite. The data was taken from the Swarm satellite during the portion of its longitudinal orbit that coincided with the Peruvian longitude. The dense Peruvian magnetometer array has been in operation since 2016, and therefore, the events that were selected were amongst those observed in 2016. In total, 33 events were selected, and the results showed good correspondence between the modeled field and the Swarm-observed field between 9 a.m. and 11 a.m. PET while discrepancies at other local times (LTs) may indicate the possibility that the current differs depending on the altitude, i.e., the current on the ground is different from that at Swarm altitude.

Using the derived model, the correlation between the estimated current density of the EEJ and the amplitude of the equatorial enhancement of the ground magnetic data was shown. Furthermore, it was shown that the width of the EEJ and the position of the EEJ axis tend to converge at a certain value when the amplitudes of the equatorial enhancement or the peak current density become larger. This kind of trend has also been reported by previous studies, and it is not inconsistent with our results. This result may indicate that the equatorial enhancement disappears and the Sq variation becomes more dominant when the amplitude of the field is small. It is possible that, for this reason, a correlation between the current density and F10.7, which is a parameter used to evaluate the strength of ionization, was not observed.

This study has a great impact on investigations into the EEJ since details of the EEJ's structure such as its width or current density are available in quasi-real time. It is expected that this model will have play an important role in space weather studies as a tool to monitor the electromagnetic structure in the ionosphere. Moreover, this study showed that our developed EEJ model reveals the possible existence of another current system at different altitudes through the comparison with the Swarm satellite data.

Acknowledgement

The author wishes to express his gratitude to his supervisor, Assoc. Prof. Akimasa Yoshikawa for his guidance during the course of this research. I’m deeply grateful for his patient supervision and much encouragement. I am also indebted to Assoc. Prof. Kawano, Assoc. Prof. Watanabe for their helpful comments and encouragement for the study during the seminar. The author is also grateful to Dr. Uozumi, Dr. Abe, and Dr. Fujimoto for their invaluable assistance in my research. Grateful thanks are expressed to all of them. MAGDAS/CPMN magnetic data were provided by the principle investigator of MAGDAS/CPMN project (http://magdas.serc.kyushu-u.ac.jp/). I also deeply thank the local corroborators of the MAGDAS project in Peru. Dr. Jose Ishitsuka, a staff of IGP, could support to develop the magnetometer array in Peru. Dr. Marco Milla and Mr. Oscar Veliz from IGP also could help a lot to maintain the instruments. Ingr. Victor Alvarado from UNAS helped us for the installation work in TMA, and could do maintenance of the instruments. The ground magnetic data at PIU, NAZ, ANC and ARE were provided by IGP. The Swarm data, which is very important in this study as well, were provided by ESA. The author express his gratitude to them.

Hiroki Matsushita
Kyushu University
2018

Table of contents

List of tables

List of figures

1. Introduction

1.1 Classical theory of the equatorial electrojet (EEJ)

A noticeably enhanced horizontal magnetic field near the dip equator during daytime has been detected by magnetometers on the ground (e.g. *Bartles and Johnston*. 1940a,b). This enhancement of the field is caused by an intense eastward electric current, which flows in the E region of the ionosphere along the dip equator, known as the equatorial electrojet (EEJ). There are generally two reasons for the highly intense EEJ: the geometry of the Earth's magnetic field lines and higher effective conductivity. The generation mechanism of the EEJ is illustrated in figure 1.1, and is explained as follows. Solar extreme ultraviolet (EUV) radiation and the ionization of the atmosphere are active in the daytime and are most active around the equator. Tidal winds in the E region of the ionosphere produce an electric field according to

$$E = U \times B \qquad (1-1)$$

where U is the velocity of the winds and B is the magnetic field. As an ion (electron) is carried by this electric field and is charged at dawn (dusk) side, the eastward electric field from dawn to dusk can be set up along the dip equator. This eastward electric field then causes a Pedersen current to flow parallel to the electric field and a Hall current to flow downwards or perpendicular to both the electric field and the magnetic field. The Pedersen and Hall currents are denoted by $\sigma_P E_x$ and $\sigma_H E_x$ in figure 1.1, respectively. The downward Hall current cannot cross the boundaries, which are in the form of non-conducting atmosphere at the bottom of the slab and effectively collisionless plasma at the top of the slab in the figure. This interruption of electric current causes the accumulation of negative charge at the top of the slab and positive charge at the bottom of the slab, that is, an upward electric field denoted by E_z in figure 1.1. Subsequently, a Pedersen current and a Hall current, which are denoted by $\sigma_P E_z$ and $\sigma_H E_z$ in figure 1.1, flow upward and eastward, respectively. The latter Pedersen current will cancel the former Hall current in a steady state, while the latter Hall current will enhance the former Pedersen current. The total vertical current and zonal current are given by equation $(1-2)$ and equation $(1-4)$, respectively:

$$J_z = \sigma_H E_x - \sigma_P E_z = 0 \qquad (1-2)$$

$$E_z = \frac{\sigma_H}{\sigma_P} E_x \qquad (1-3)$$

$$J_x = \sigma_P E_x + \sigma_H E_z = \sigma_C E_x \qquad (1-4)$$

where σ_c is the Cowling conductivity (*Hirono*, 1950a,b; *Hirono*, 1952; *Hirono*, 1953), which is defined as $\sigma_c \equiv \frac{\sigma_H^2+\sigma_P^2}{\sigma_P^2}$. Since the generation of the vertical electric field proceeds most efficiently at the dip equator, where the magnetic field lines are perpendicular to the boundaries, and Cowling conductivity is at a maximum around the equator owing to the ionization by EUV radiation, the observed enhancement is also at a maximum at the equator. The resulting strong eastward electric current is called the EEJ, which is generally described to flow in the narrow region between -3 and 3 degrees of dip latitude, and produces a noticeably enhanced ground magnetic field.

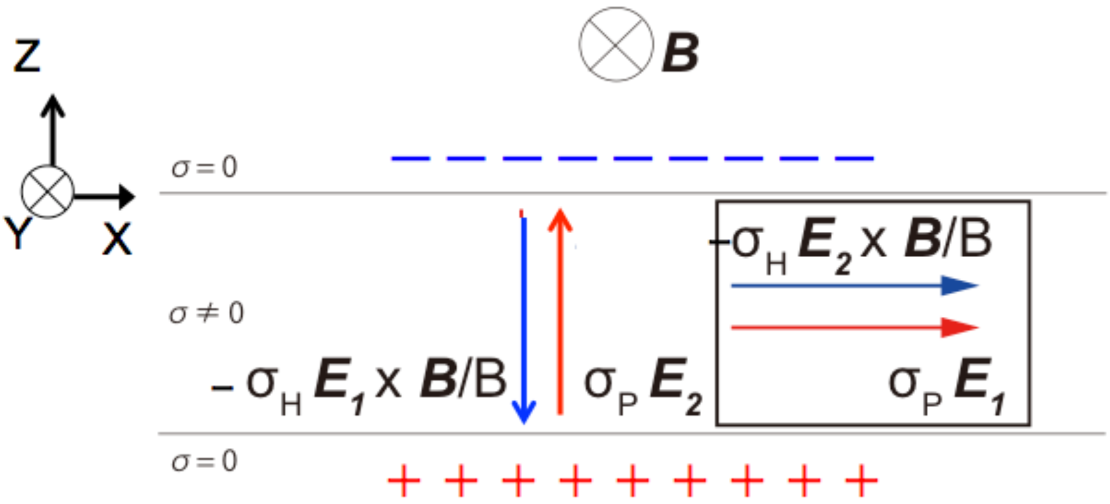

Figure 1.1 A schematic of the generation mechanism of the EEJ, where E1 and E2 represent the eastward electric field and the vertical polarization electric field in the ionosphere. σ_H and σ_P are the Hall conductivity and the Pedersen conductivity, while B represents the line of the force of magnetic field

1.2 Reviews of EEJ studies

Although the basic generation mechanism of the EEJ can be explained as in section 1.1, there are still interesting features of the EEJ, such as local time (LT) variation/long-term variation/day-to-day variability of the amplitude, the longitudinal dependency of the EEJ, and the structure of EEJ that require investigation. Accordingly, the past studies related to these features are introduced in the following subsections for each different method or tool.

1.2.1 Ground magnetic data

As mentioned above, the equatorial enhancement was originally noticed in ground magnetic data. Later, *Chapman* (1951) reported that the large range of the horizontal component of the daily variation in the magnetic field at Huancayo indicates the existence of an intense eastward current above it, which he named the EEJ. Since the advantage of ground magnetic data for EEJ studies is temporal variation, the relationship between the range of the horizontal component and the solar activity or its seasonal dependency has been investigated in various papers. *Yamazaki et al.*, (2010), using 10 years of datasets, revealed good correlation between F10.7, which is well known as the proxy of solar EUV radiation, and the EEJ variation at Davao in the Philippines whose dip latitude is -0.84 degrees. They found the correlation coefficient to be 0.53. They also found predominant semiannual variation of the EEJ, that is, the peak amplitude could be seen in spring and in fall. This feature was also reported by *Stening* (1995a), and it is explained as the effect of both semiannual changes in ionospheric conductivity (*Wagner et al.*, 1980) and diurnal tidal wind fields in the middle atmosphere (*Burrage et al.*, 1995). Moreover, *Fujimoto et al.*, (2016) also investigated the relationship between F10.7 and the EEJ variation at Ancon in Peru including a geomagnetically disturbed day using the EE index which was introduced by *Uozumi et al.*, (2008) as an index to monitor EEJ activity. They found that they had similar trends. It should be noted that *Yamazaki et al.*, (2010) and *Fujimoto et al.*, (2016) used the daily range of the northward component as the EEJ variation without separating the global-Sq field and the local-EEJ field. Meanwhile, *Hamid et al.*, (2013) found that the correlation coefficient between F10.7 and the EEJ variation in the Philippines was 0.43, which was calculated using the two-station method wherein the field outside of the dip equator was subtracted from the field at the dip equator.

1.2.2 Low Earth Orbit (LEO) satellite magnetic data

It is difficult to use LEO magnetic data to investigate the temporal variation of the EEJ at a particular location since the LEO satellites orbit different longitudes with every rotation.

They do, however,they moves through very fast in every orbit very quickly. Therefore, it can be said that the LEO data observe a kind of snap shot of the latitudinal profiles, that is, spatial variation. In addition to the spatial variation, the aspects of the EEJ structure, such as the current density or intensity and the width of the EEJ also can also be estimated using by LEO data. The EEJ variation in the LEO data was observed as a negative depression of the magnetic field of northward component since satellites orbit above eastward flowing EEJ, and the observations by Polar Orbiting Geophysical Observatory (POGO) satellites had revealed such characteristics (*Cain and Sweeney*, 1973; *Onwumechili and Agu*, 1980, 1981a,b). *Jadhav et al.,* (2002) studied the EEJ current structure in detail using the Ørsted satellite data, and they found an average height-integrated current density of around 0.20 A/m and very large dispersion of the width of the EEJ. On the other hand, *Luhr et al.*, (2004) found that the current density was 0.15 A/m using the measurements from the CHAllenging Minisatellite Payload (CHAMP) satellite, which is smaller than the value found by *Jadhav et al.,* (2002). They concluded that this discrepancy was due to different current models being adopted As they adopted a series of line current as the EEJ while *Jadhav et al.,* (2002) adopted a continuous distribution of current as the EEJ. The width of the EEJ estimated by *Luhr et al.*, (2004) showed smaller deviation than previous results (*Jadhav et al.*, 2002; *Onwumechili*, 1967). They mentioned that previous studies included a geometric effect since the EEJ is tilted in a certain area. As for the relationship between the width and the peak current density, *Luhr et al.*, (2004) revealed that the width of the EEJ becomes larger with higher amplitudes of the peak current density while *Onwumechili and Agu*, (1981b) reported an inverse trend. *Luhr et al.*, (2004) also found that the close linear relationship between the current density and the current intensity was not constant. Therefore, they concluded that larger currents could flow at longitudes with larger Cowling-channel cross sections.

1.2.3 In-situ sounding rocket-borne observation data

Rocket measurements allow the height profile of the EEJ to be studied while it is difficult to obtain the temporal and spatial variations. *Maynard and Cahill*, (1965) performed rocket experiments over the dip equator in India, and they found the peak current density at 105 km and 109 km during the ascent and descent, respectively. The lower edge and upper edge of EEJ current density were also detected in their study at 89 km and 136 km from the ground, respectively. *Shuman,* (1970) also performed a rocket experiment near the dip equator in Peru, and found that the peak amplitude of the current density was observed at 106 km. *Onwumechili*, (1992d) revealed a linear relationship between the width of the EEJ and the peak current density, that is, the larger (smaller) the amplitude of the peak current density, the thicker (thinner) the EEJ will be.

1.3 Temporal variation of the EEJ

As mentioned above, the use of ground-based magnetic data has an advantage for studying the temporal variation of the EEJ. Hereafter, this temporal variation is briefly introduced. LT variations of the normal EEJ and time developments of the EEJ during a storm/substorm are used to represent the temporal variation of the EEJ during a quiet time and a disturbed time, respectively.

1.3.1 LT variation during a quiet time

The observation of the EEJ variation on the ground, which is an abnormal enhancement of the amplitude of the daily magnetic variation, started in 1922 at Huancayo, Peru by the Department of Terrestrial Magnetism of the Carnegie Institution of Washington. Chapman (1951) explained the feature of LT variation of the EEJ as follows; "the S_q(H) variations during the night are small, and during the day they consist of a rise to and a fall from maximum value at about 11 a.m." Although the "S_q(H)" in *Chapman* (1951) included both the local-EEJ field and the global-Sq field, *Manoj et al.* (2006) also revealed in their paper that the local-EEJ field derived from the difference between values obtained from magnetometer observatories located near the dip equator and off the dip equator showed a similar variation, which is the peak at 11 a.m.

1.3.2 Time developments of the EEJ during a disturbed time

The response of low-latitude electrodynamics to high-latitude geomagnetic activity such as a substorm has been studied using plasma drift measurements at Jicamarca (*Fejer and Scherliess* (1995); *Scherliess and Fejer* (1997)) as well as ground-based measurements (*Kelley et al.*, (1979); *Gonzales et al.*, (1979); *Wei et al.*, (2012)). *Yamazaki and Kosch* (2015) examined the response of the EEJ to geomagnetic storms and substorms using long-time series of ground magnetic data since such a response in daytime had not been well studied, statistically. In the paper, they sorted the substorm effects according to the time history of the AE index, which is an index to represent the relative amplitude of substorm provided by World Data Center (WDC) for Geomagnetism, Kyoto, and found that the EEJ was enhanced when the AE index decreased suddenly, which indicated the penetration of a high-latitude convection electric field (c.f. *Nishida*, 1968). They also suggested that the westward EEJ followed by the disappearance of the enhanced EEJ in an hour indicated the existence of disturbance dynamo (c.f. *Blanc and Richmond*, 1980). Similarly, they also concluded that the westward disturbances of the EEJ during the recovery phase could also be explained by disturbance dynamo. However, the position of the westward disturbance of the EEJ was not revealed since they used data from only one station for the dip equator at a particular longitude.

1.4 The models of the EEJ current and its magnetic field

Originally, *Chapman* (1951) proposed three types of electric-current models for the EEJ current. These were the line current model, the current ribbon of constant intensity model, and the current ribbon of parabolic intensity model. Subsequently, the current ribbon of triangular intensity model and the current ribbon of fourth-degree intensity model were introduced by *Suzuki and Maeda* (1968) and *Fambitakoye and Mayaud* (1976a), respectively. *Onwumechili* (1965a,b) then introduced the continuous distribution of current density model. These models and their magnetic fields are briefly introduced in this section.

1.4.1 Models proposed by Chapman (1951)

At first, an infinitely long straight current was assumed for the EEJ in his study. The lines of force produced by a current of this type are circles around the axis, and are described as follows

$$B = \frac{0.2I}{r} \qquad (1-5)$$

where I is total intensity of the current, and r is the distance from the axis. Accordingly, the horizontal component H and the vertical component Z are given by

$$H = \frac{0.2Iz}{(x^2 + z^2)} \qquad (1-6)$$

$$Z = \frac{0.2Ix}{(x^2 + z^2)} \qquad (1-7)$$

where z is the height of the current while x is the distance from the axis to the north. Chapman (1951) then suggested "a band of uniform current flow" as a more realistic model of the EEJ. In other words, he suggested the current ribbon of constant intensity model in which the current has a width of 2w in the north-south direction and flows eastward. The horizontal component H and the vertical component Z produced by this current are derived from

$$H = 0.2J \tan^{-1} \frac{2wz}{x^2 + z^2 - w^2} \qquad (1-8)$$

$$Z = 0.1J \ln \frac{z^2 + (x-w)^2}{z^2 + (x+w)^2} \qquad (1-9)$$

where J is the sheet current density with the units of A km^{-2} and x and z are the distances from the axis to the north and upward, respectively. Finally, he suggested "a distributed band of unidirectional current" as the most realistic model of the EEJ. In this model, using the width of current or the latitudinal extent of the current defined by $2w$, and J_0 which is the peak current density at x=0, the model current density J at the point y is given by

$$J = J_0 \left(1 - \frac{y^2}{w^2}\right) \qquad (-w \le x \le w) \qquad (1-10a)$$

$$J = 0 \qquad (x \ge w, x \le -w) \qquad (1-10b)$$

Therefore, the magnetic field change of the horizontal component and the vertical component produced by this current at the point (x, z) are given, respectively, by

$$H = 2J_0 z \int_{-w}^{w} \frac{(1 - y^2/w^2)}{z^2 + (x-y)^2} dy \qquad (1-11a)$$

$$Z = 2J_0 \int_{-w}^{w} \frac{(1 - y^2/w^2)(z-y)}{z^2 + (x-y)^2} dy \qquad (1-12a)$$

If

$$\tan \theta_1 = \frac{z-w}{h}, \qquad \tan \theta_2 = \frac{z+w}{h},$$

Equations (1 – 11a) and (1 – 12a) can be transformed as follows

$$H = \frac{3C}{2w^3}\left\{(w^2 - x^2 + z^2)(x_2 - x_1) + 2xz \ln\frac{\sec\theta_2}{\sec\theta_1} - z^2(\tan\theta_2 - \tan\theta_1)\right\} \quad (1-11b)$$

$$Z = \frac{3C}{2w^3}\left\{(w^2 - x^2 + z^2) \ln\frac{\sec\theta_2}{\sec\theta_1} - 2xz(\theta_2 - \theta_1) + 2xz(\tan\theta_2 - \tan\theta_1) - \frac{1}{2}z^2(\tan^2 x_2 - \tan^2 x_1)\right\} \quad (1-12b)$$

where $C = 4wJ_0/3$.

1.4.2 The current ribbon of triangular/fourth-degree intensity models

Suzuki and Maeda (1968) proposed the triangular-shaped current, which is shown in figure 1.2, as a simple model of the EEJ, and discussed its reliability by comparing it with theory and rocket measurements. They suggested in the paper that the results of the rocket measurements by *Davis et al.* (1967) and the theoretical model of the EEJ by *Untiedt* (1967) could be approximated to a triangular structure of the EEJ from north southward. They also noted, however, that the triangular model could not represent a return current of the EEJ, which had been mentioned in previous papers (e.g. *Chapman*, 1951; *Onwumechili*, 1967; *Maynard*, 1967). Therefore, they concluded that their model could be regarded as a simplified version of the one by *Onwumechili* (1967). *Fambitakoye and Mayaud* (1976) proposed the “fourth-degree distribution current model” for the EEJ. In this model, the current density at $x,$ which is the distance from the axis to the north, is given by

$$J(x) = J_0\left(1 - \frac{(x - x_0)^2}{a^2}\right)^2 \quad (1-13)$$

where x_0 is the position of the axis, and a is the half-width of the current. They confirmed the reliability of the model by comparing the model with the numerical model of the EEJ presented by *Richmond* (1972), and obtained a very similar latitudinal structure as shown in figure 1.3, which is taken from *Fambitakoye and Mayaud* (1976). Moreover, they indicated that smaller residuals between Richmond’s model and the fourth-degree current model could be seen than those between Richmond’s model and the parabolic model.

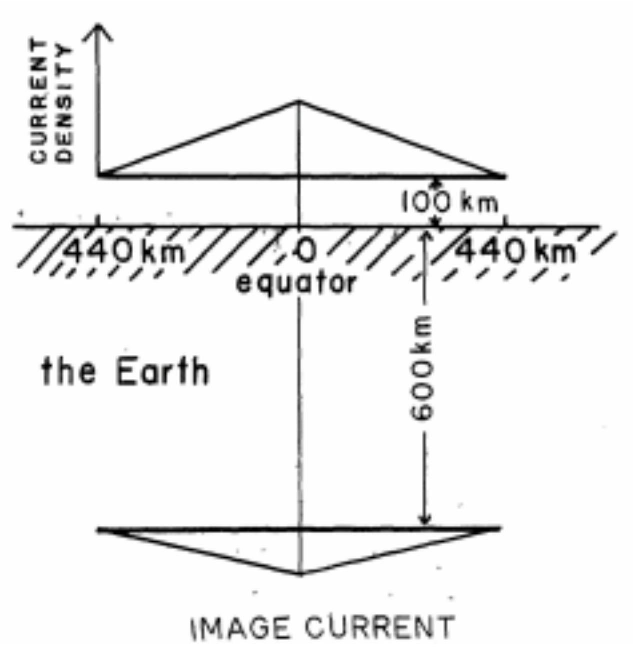

Figure 1.2 The schematic of the triangular EEJ model (taken from *Suzuki and Maeda*, 1968)

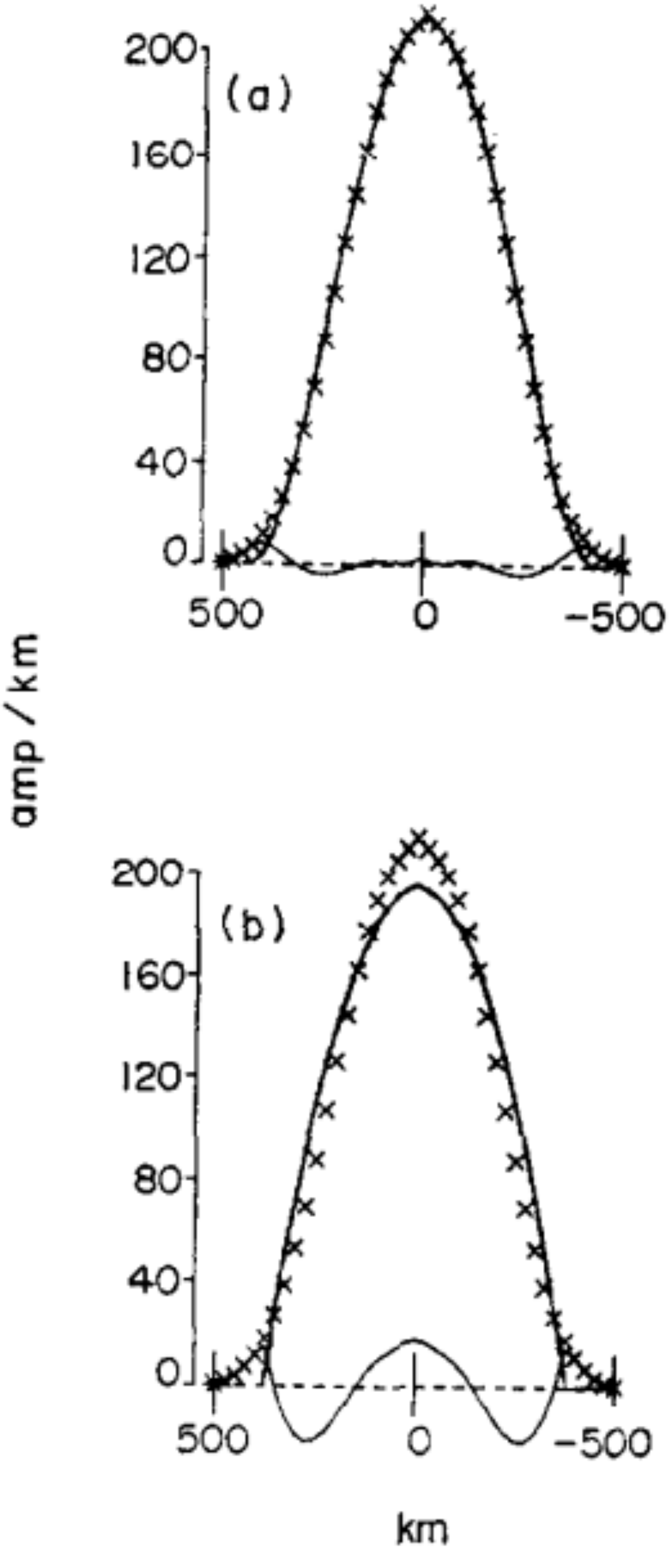

Figure 1.3 The latitudinal profile of Richmond's EEJ model (indicated by crosses in both of panels) with the latitudinal profiles of (a) the fourth-degree intensity model, and (b) the parabolic intensity model (taken from *Fambitakoye and Mayaud*, 1976)

1.4.3 The continuous distribution of current density model

Although *Chapman* (1951) originally suggested three types of models for the EEJ current, *Onwumechili* (1965a,b) stated that none of Chapman's models described the equatorial enhancement observed on the ground well and subsequently introduced the "two-dimensional continuous distribution of current density model" as a new model for the EEJ. There are two advantages of this model; the one is the ability to represent the return current of the EEJ. The other is that it is two-dimensional, that is, it describes the *x*-*z* plane, which means that this model is also useful to explain rocket measurements. The current density j (A km^{-3} for this model at the point (x, z) is given by

$$j = j_0 \frac{a^2(a^2 + \alpha x^2)}{(a^2 + x^2)^2} \frac{b^2(b^2 + \beta z^2)}{(b^2 + z^2)^2} \hat{y} \qquad (1-14)$$

where j_0 is the peak current density at $x = 0, z = 0$; a and b are the constant scale lengths along x and z, respectively; and α and β are dimensionless constants which control the shape of the current along x and z, respectively. Figure 1.4 shows some examples of the latitudinal distribution of this current density from *Onwumechili* (1965a,b).

1.5 Purpose of this paper

As described previously, there are few studies investigating the latitudinal profile of the EEJ temporally. Hence, the characteristics of the daily magnetic field that change around the dip equator, such as which structural change of the EEJ current contributes to the long-term variation or LT variation are not clear. Accordingly, the dense Peruvian ground-magnetometer array was developed in order to monitor the latitudinal profile of the EEJ continuously. The methodology, containing the model construction and procedure for extracting the EEJ-related magnetic data on the ground, is described in Chapter 2. Chapter 3 details the results of the evaluation of the model using LEO data. The results of the long-term variation of the EEJ structure in 2016 are presented in Chapter 4. Chapter 5 details the LT variations of the EEJ structure during a normal EEJ, a counter EEJ, and a magnetic storm. Finally, the summary and conclusions are presented in Chapter 6 along with the future prospects for research using this EEJ model.

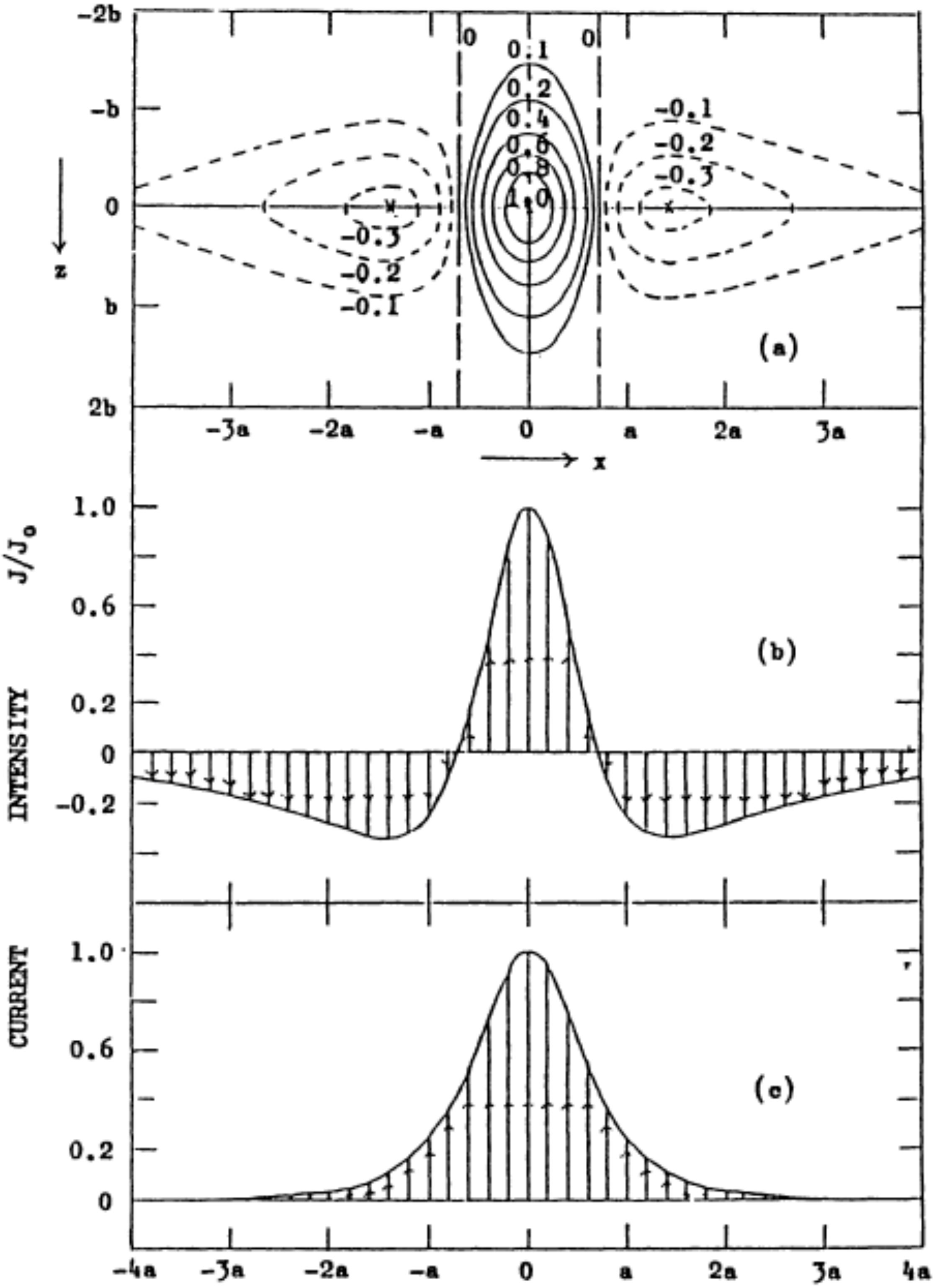

Figure 1.4 (a) A contour plot of the EEJ current density (A km^{-2}) relative to the peak density (A km^{-2}) for $\alpha = -2, \beta = 0$, where eastward (westward) current is denoted by solid (broken) contour lines. (b) A latitudinal variation of the EEJ current density for $\alpha = -2$. (c) Same as (b) but for $\alpha = 0$ (taken from *Onwumechili,* 1965a,b)

2. Methodology

The EEJ structure, which relates to the width, shape, and total intensity of the EEJ, was estimated by solving the inverse problem of relating the physical models of the magnetic field to the observed magnetic data from the dense magnetometer array near the dip equator in Peru. Each model was produced by changing various parameter values, and the method of least squares was applied to determine which model best described the data. Sections 2.1 and 2.2 explain the details of the models and data from the ground magnetometer array used in this study, respectively.

2.1 The model for the EEJ

In order to estimate the EEJ structure, the continuous thin current shell model (*Onwumechili,* 1992) was used as the EEJ model and is given by equation $(2-1)$

$$j = J\frac{a^2(a^2+\alpha x^2)}{(a^2+x^2)^2} \qquad (2-1)$$

where $\alpha, a, J,$ and x express the shape of the current along the meridional line, the latitudinal width of the current, the height-integrated current density at the current axis and the northward distance from the position of the current axis, respectively. The northward and vertical magnetic fields produced by this current are given by equation $(2-2)$ and $(2-3)$, respectively, by solving the equation $(2-1)$ according to Biot-Savart's law:

$$-|z|X = \frac{1}{2}Ka\frac{(v+\alpha v+2\alpha a)(u+b)^2+(v+\alpha v+2a)(v+a)^2}{[(u+b)^2+(v+a)^2]^2} \qquad (2-2)$$

$$-|x|Z = \frac{1}{2}Ka(u+b)\frac{(1+\alpha)(u+b)^2+(v+\alpha v+3a-\alpha a)(v+a)}{[(u+b)^2+(v+a)^2]^2} \qquad (2-3)$$

where K is the constant value, which is described by $K = 0.2\pi J$; $u(v)$ is the absolute value of $x(z)$, which is the northward (vertical) distance from the current axis. The variable b is the vertical scale of the current, which is assigned to be zero in this study, and α, a, J are defined in the same way as equation $(2-1)$. The model magnetic fields in equation $(2-2)$ were calculated by substituting values from -10 to 0 in steps of 0.1 for α; values from 200 to 1000 in steps of 10 for a; and values from 0 to 400 in steps of 1 for J. The set of values that best explained the EEJ structure obtained from the ground magnetic data using the method of least squares was determined. Figure 2.1 and figure 2.2 display examples of the model-calculated current and magnetic fields for different values of the parameters J, a, α from left to right. It should be noted that for each parameter that varies, the other parameters remain at constant values. As figure 2.1 and figure 2.2 indicate, higher values of a and J contribute indicate a wider and higher-density current or amplitude of the magnetic field, and vice-versa. On the other hand, a trend for the contribution of α to the current structure is not specifically observed but negative values shape the return current of EEJ.

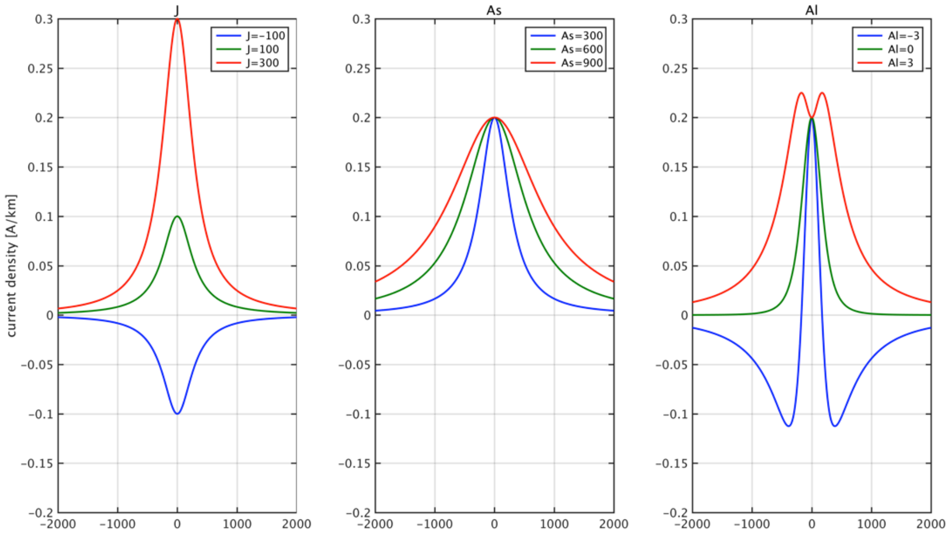

Figure 2.1 Calculated current models for different parameters, where peak current density is varied on the left, the parameter related to width is varied in the middle and the parameter related to the shape is varied on the right

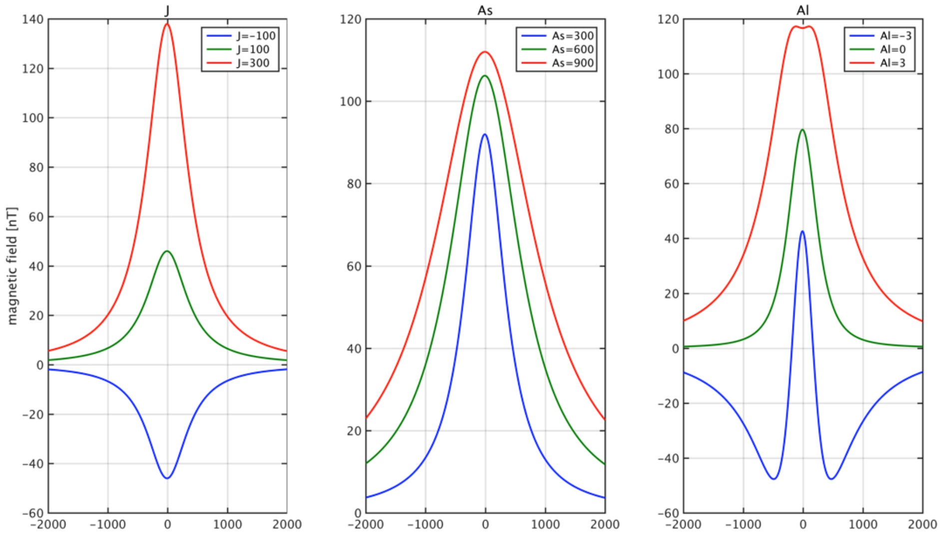

Figure 2.2 Calculated models of the magnetic fields on the ground for different parameters varied in the same manner as in figure 2.1

2.2 Ground magnetic data

The magnetic data on the ground used in this study were provided by the MAGnetic Data Acquisition System/Circum-pan Pacific Magnetometer Network (MAGDAS/CPMN) Group and the Institute del Geo Physico (IGP). Both datasets are available at 1-second and 1-minute time resolution, but 1-hour averaged data of the 1-minute data were used in this study. As shown in Figure 2.3, seven stations located near the dip equator were mainly used, and the location of every stations and of the dip equator is shown by blue-colored circle and a red-solid line, respectively. The red broken lines in the figure show the positions of the edges of the EEJ as mentioned by previous researchers (*Onwumechili*, 1992). The information for every station is also summarized in Table 2.1. As the original data of the magnetic field include various effects such as the Sq current, the main field of the Earth, and the magnetospheric current, the effect of the EEJ had to be extracted. In order to remove these extraneous effects, the magnetic data at Piura, the mean values of the magnetic data from each station for the nighttime between 6 p.m. and 6 a.m., LT in a day and the Dst index, which was introduced by *Sugiura & Kamei*, (1981) as an index for monitoring the global disturbed magnetic field of the earth, were used in this study for the variation of the Sq current, the main field and the magnetospheric current, respectively. The modified Dst index according to the location of each station was calculated by

$$B_{Dst}^{*} = B_{Dst} \cdot \cos(\theta_d)$$

where B_{Dst} is original value of the Dst index and θ_d which is zero at the dip equator where the magnetic field line of the earth is horizontal, is the dip latitude of the stations. As there is insufficient ionization to produce an ionospheric current during the nighttime because of little or no solar radiation, and the effect of ring current is subtracted by the modified Dst index, the nighttime magnetic field can be used as the main field of the Earth.

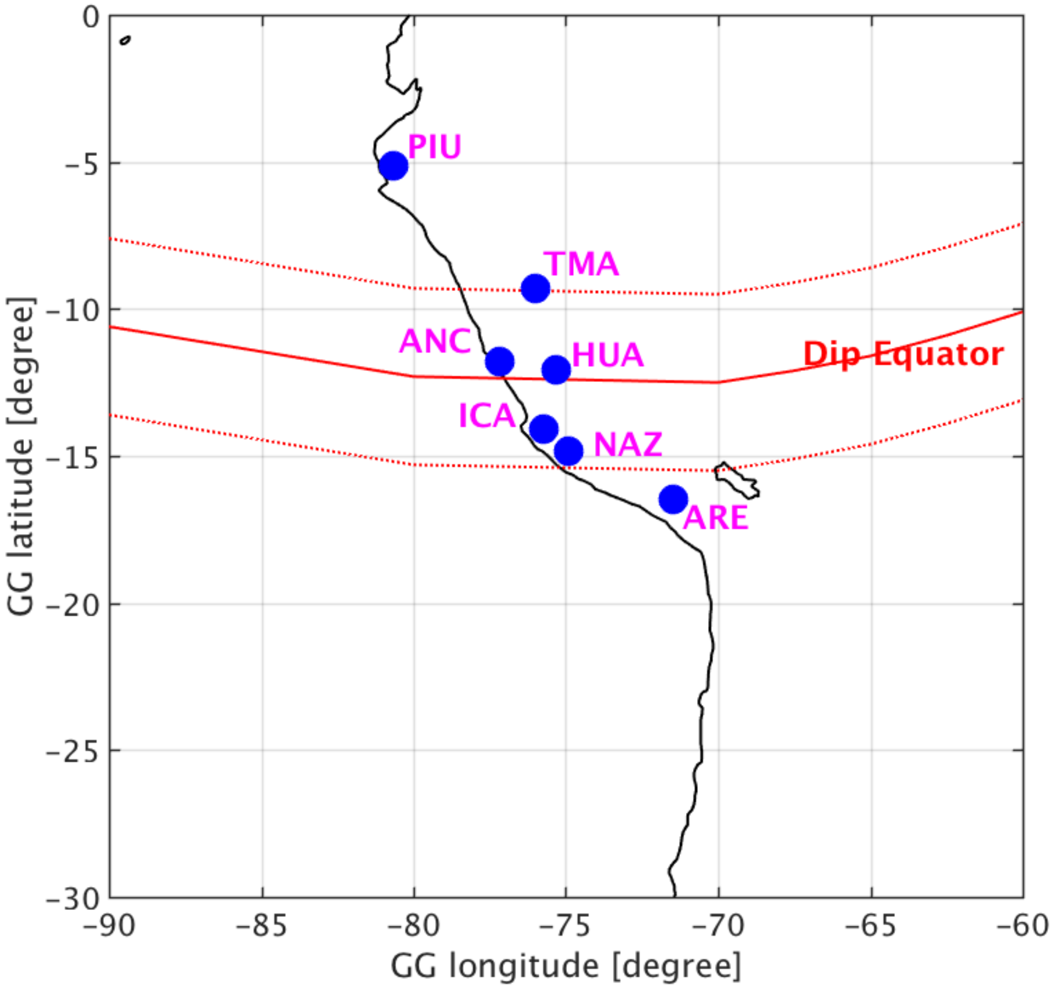

Figure 2.3 Map of the stations that supplied the magnetic data for this study

Station ID	Name	GG lat.	GG lon.	GM lat.	GM lon.	Dip lat.
PIU	Piura	-5.14	-80.67	4.44	-7.93	6.58
TMA	Tingo Maria	-9.31	-76.00	0.37	-3.23	2.61
ANC	Ancon	-11.77	-77.15	-2.09	-4.33	0.14
HUA	Huancayo	-12.02	-75.29	-2.32	-2.50	-0.14
ICA	Ica	-14.09	-75.74	-4.38	-2.93	-1.84
NAZ	Nazca	-14.83	-74.92	-5.11	-2.12	-4.61
ARE	Arequipa	-16.47	-71.49	-6.74	1.20	-3.51

Table 2.1 List of the stations that supplied the magnetic data used in this study

3. Test of the appropriateness of the estimation of the EEJ structure

In this chapter, the EEJ structure estimated from the ground-based magnetic data is compared with the magnetic data derived by a polar low Earth-orbiting satellite. A brief introduction of the LEO satellite used in this study and the procedure used to extract the EEJ variation from the LEO magnetic data are described in section 3.1; then results of the comparison are shown in section 3.2. Lastly, the discussion regarding the results is provided in section 3.3.

3.1 LEO satellite magnetic data

The low earth orbit is defined as the region of space below an altitude of 2000 km according to the guidelines published by the National Aeronautics and Space Administration (NASA) in 1995. Furthermore, its orbital period is between 84 and 127 minutes. In addition to the altitude, the inclination of the satellite, which is the angle of the orbit in relation to the Earth's equator, is also an important parameter. Figure 3.1 illustrates the inclination of an orbit, where the red arrow indicates the orbit, and the black two-way arrow indicates the inclination. The inclination is zero when the orbit of the satellite is just above the equator and it is 90 degrees when the orbit passes from the geographic North Pole to the South Pole. The orbit just above the equator is interesting since the satellite remains in one spot on the Earth while the polar orbit, where the inclination is 90 degrees, is also interesting because the satellite remains at one time. Therefore, many polar-orbit satellites were launched for the purpose of, for example, establishing the longitudinal dependency of the EEJ at the same LT as mentioned in section 1.2 of Chapter 1.

The polar orbital satellite magnetic data were used here in order to focus on the latitudinal structure of the EEJ at a fixed LT. It should be noted that the Swarm satellites were used in this study. The magnetic data from the Swarm satellites are available from the European Space Agency (ESA) 's website (https://earth.esa.int/web/guest/swarm/data-access). The Swarms, which consist of three satellites, namely, Swarm A, Swarm B, and Swarm C, were launched in November 2013. They are equipped with two types of magnetometer, a vector-field magnetometer and an absolute-scalar magnetometer, but only Swarm A and its vector-field magnetometer were used here. Moreover, this vector-field magnetometer is a fluxgate magnetometer, and although it has two settings of 50 Hz and 1 Hz for the sampling rate, only the 1 Hz data were used. The coordinate system of the magnetic data is the NEC system, where N, E, and C correspond to North, East, and Center, respectively.

As the magnetic data obtained by the Swarm satellites include not only a variation produced by the EEJ but also by the main field of the Earth, the variation from a Sq current or a magnetospheric current amongst others, the variation caused by only the EEJ must be extracted. However, it is not easy to separate the observed magnetic data itself into its contributing variations because the variation or field is recorded on the magnetometer as the combined value. In spite of this, the International Geomagnetic Reference Field (IGRF) model field and interpolation field between the fields at the off-dip equators, generally known to be at plus and minus 12 degrees away from the dip equator, were applied to the main field and the variation originating from the Sq current, respectively. Furthermore, it was assumed that the magnetic field caused by the magnetospheric current was relatively small in the case where geomagnetic activity is quiet, i.e., when the Kp index is less than 3. Figure 3.2(a) shows the averages of the northward magnetic field from the IGRF model and the Swarm observation along a Swarm orbit during the period between 10 a.m. and 2 p.m. LT and between the 70th and 80th meridians west. The green-line plot in the figure shows the IGRF-modeled main field, while the blue-line plot shows the Swarm-observed magnetic data. The plots seem to be identical in the scale of tens of thousands of nanoteslas. The residual variation, which is the IGRF field subtracted from the Swarm magnetic data, was calculated to see the difference between them in a fine scale. The result is displayed in figure 3.2(b). As the residual does not show abnormal values such as outliers or gaps, it can be said that the application of the IGRF-modeled field as the main field observed by the Swarm is valid.

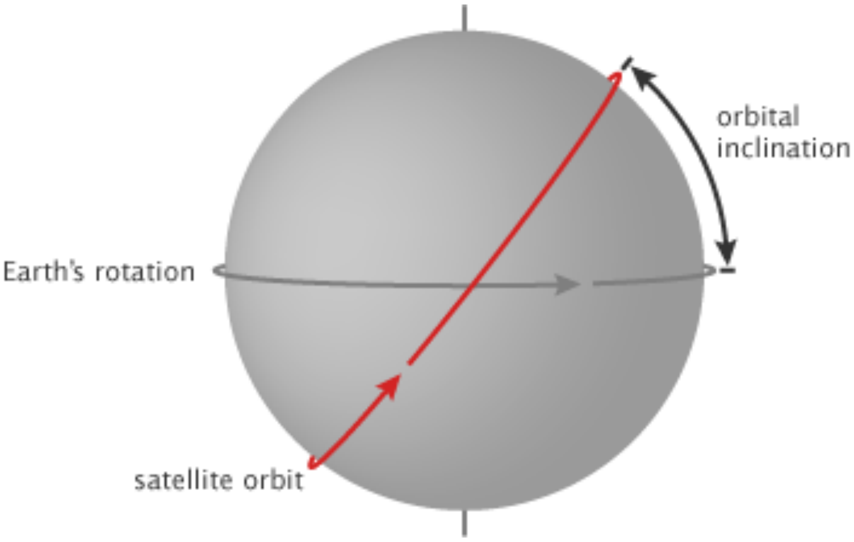

Figure 3.1 Illustration of an orbital inclination (taken from "Catalog of Earth Satellite Orbits" by NASA)

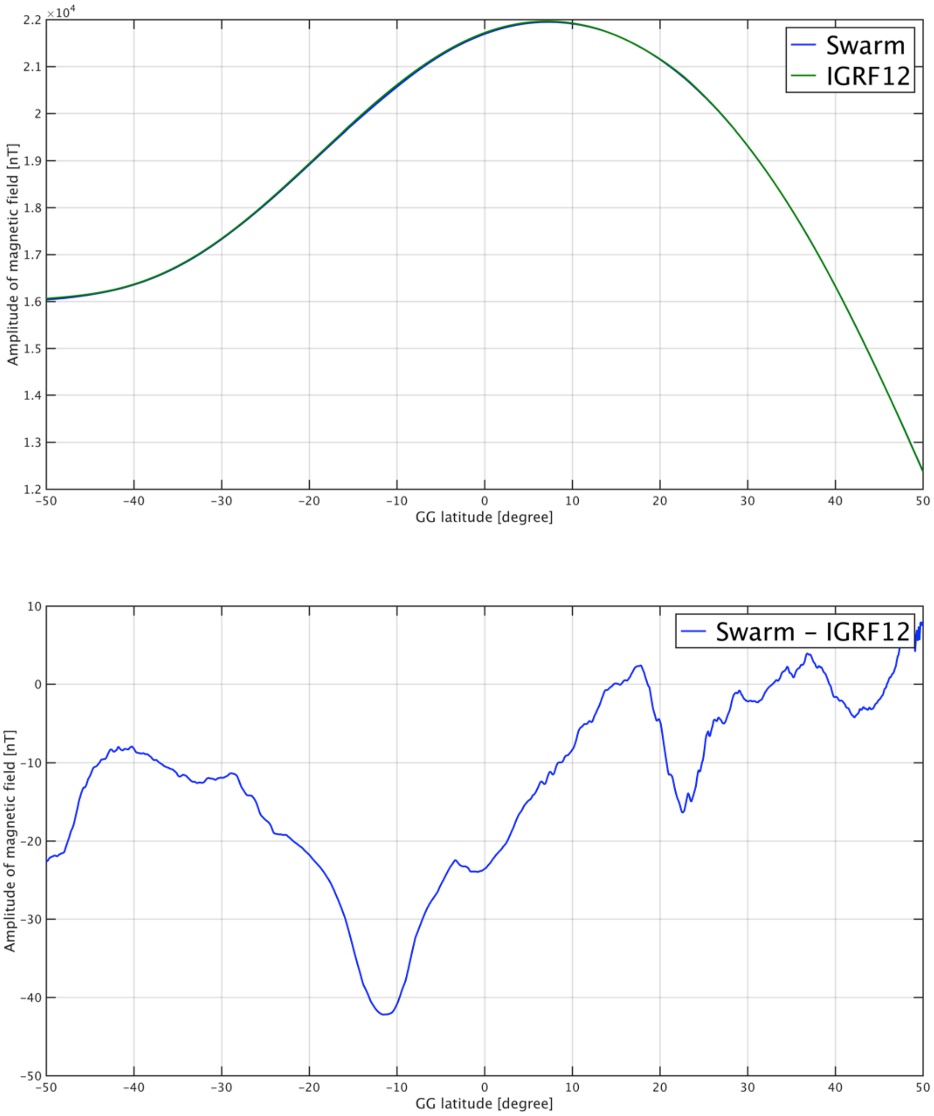

Figure 3.2 A northward magnetic field observed by Swarm (blue) and that modeled by IGRF12 (green) averaged between 10 a.m. -2 p.m. LT and between geographic longitudes of -70 and -80, where the minus indicates a westward direction (top), Residual between the observations by Swarm and the IGRF12-modeled data (bottom).

3.2 Comparison with the observed data at the LEO-satellite altitude

As mentioned at the beginning of this chapter, the estimated EEJ structures from ground-based magnetic data were compared with the LEO-observed magnetic data in order to confirm the validity of the estimated structure. Both datasets used in this study are for the period between January 1 and December 31, 2016. Firstly, the LEO data, whose orbital longitudes are the Peruvian longitudes, that is, those between -80 and -70 degrees of geographic longitude, were extracted from all of the data from 2016. Then, the EEJ structure during each orbit was estimated from the quasi-simultaneous ground-based magnetic data. Furthermore, the magnetic fields at the orbital altitude were calculated from the EEJ structures according to Biot-Savart's law, and they were then compared with the observed LEO data. The events whose available ground magnetic data were less than three stations were excluded. Ultimately, 33 orbits were extracted between the LTs of 8 a.m. and 4 p.m. They are listed in Table 3.1, where LT of the orbit and N_STN indicate the LT of the orbits and the numbers of available stations, respectively. The orbital longitude in Table 3.1 is the one of the geographical coordinates.

LT of orbit (hour)	Orbital longitude (degree)	Date	N_STN
08	−71.16 ± 0.31	Apr 17	5
	−77.35 ± 0.31	Aug 30	4
09	−72.12 ± 0.31	Apr 06	7
	−71.90 ± 0.31	Apr 08	5
	−79.57 ± 0.31	Aug 18	5
	−71.84 ± 0.31	Dec 29	4
10	−72.92 ± 0.31	Mar 25	6
	−72.73 ± 0.31	Aug 07	6
11	−73.39 ± 0.31	Mar 13	4
	−73.25 ± 0.31	Mar 16	6
	−76.57 ± 0.31	Jul 26	6
	−76.00 ± 0.31	Dec 06	4
12	−73.78 ± 0.31	Mar 01	6
	−73.71 ± 0.31	Mar 04	5
	−70.78 ± 0.31	Jul 14	7
13	−73.90 ± 0.32	Feb 21	5
	−72.86 ± 0.31	Jul 03	7
	−72.35 ± 0.31	Nov 16	4
14	−73.80 ± 0.32	Feb 09	5
	−73.86 ± 0.32	Feb 12	6
	−74.35 ± 0.31	Jun 21	6
	−73.86 ± 0.31	Jun 24	6
	−72.06 ± 0.31	Nov 02	5
15	−73.35 ± 0.31	Jan 28	6
	−73.49 ± 0.31	Jan 31	5
	−76.23 ± 0.31	Jun 09	5
	−75.78 ± 0.31	Jun 12	4
	−75.51 ± 0.31	Oct 21	6
	−74.67 ± 0.31	Oct 24	5
16	−72.66 ± 0.31	Jan 19	5
	−72.86 ± 0.31	May 31	5
	−77.55 ± 0.31	Oct 12	6

Table 3.1 Events list for comparison with LEO data

3.2.1 Case 1: February 12, 2016 at 2 p.m. LT

In figure 3.3, the left panel shows the LT variation of the northward component of a 1-hour magnetic field on the ground on February 12, 2016. The different colors of the plots indicate the data taken by the different stations, where the Station ID denoted in the figure. The orbital time of the Swarm satellite is indicated by the vertical black dashed line in the left panel, that is, 2 p.m. LT in Peru. The right panel shows the locations of the stations and the Swarm's orbit by blue-colored circles and a black dashed line, respectively. The red solid line and red dashed lines indicate, respectively, the dip equator and the typical edges of the EEJ, which are well known to be located at $\pm 3°$ of latitude from the dip equator. As explained in Chapter 2, latitudinal profile of the magnetic field change as a result of the EEJ for this case was estimated using ground magnetic data and Swarm data. They were then compared and the comparison is presented in figure 3.4, where the x-axis and y-axis correspond to the geographic latitude on the 75th meridian West and the magnetic field variation produced by the EEJ, respectively. The model field and the observed values are indicated by a black solid line and red-colored stars in the figure, respectively. The model and the observed values for case 1 match each other well except for the value at ARE, which is the first data point from the left. As shown by the gray-colored plot in figure 3.3, it is unlikely to be due to an error in the data. Although there is the possibility of a return current above the ARE station, another possibility is the effect of the local current such as the induced current along the coastline. The effect of an induced current will be discussed in later sections. Subsequently, the modeled field for this ground magnetic data at the altitude of the Swarm satellite is presented in figure 3.5 along with actually observed value. The blue- and green-colored plots indicate the modeled and the observed fields, respectively, where the x-axis is the geographic latitude. Although an increase in the modeled field was observed at the Swarm's altitude, it was still approximately 10 nT smaller than the observed value. Moreover, the estimated current structure from ground magnetic data and Swarm data are shown in the figure 3.6 by blue-colored and green-colored plots, respectively. The peak values of the current density were estimated as 0.084 A m^{-2} for the ground-based estimate and 0.134 A m^{-2} for the Swarm-based estimate. The parameters for the current shape and width, namely α and a were estimated as -0.80 and 310 for the ground data and -0.50 and 290 for the Swarm data. The width of the EEJ estimated from the ground data is narrower than the one estimated from the Swarm data. The values for the former and the latter were 3.11 degrees and 3.68 degrees, respectively, as calculated by $w^2 = -a^2/\alpha$. The way in which the differences in the width or the peak current density affect the modeled field will be discussed in later sections.

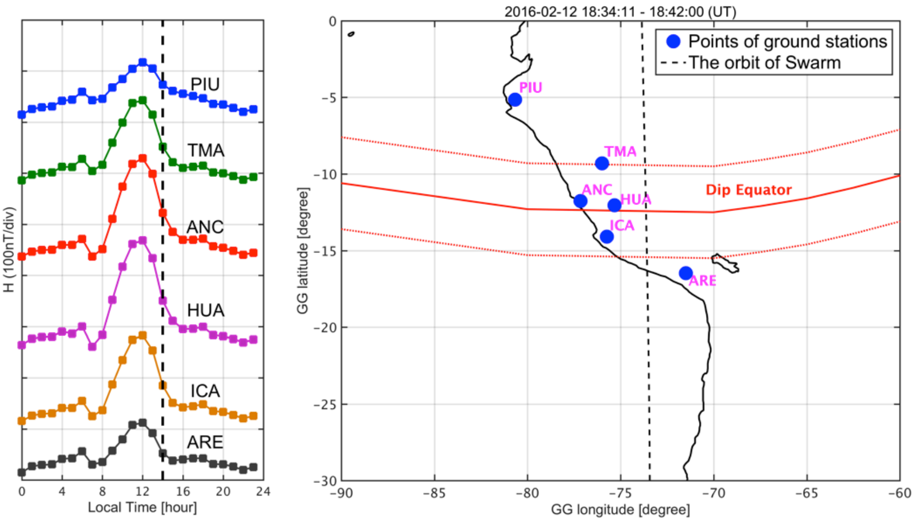

Figure 3.3 Daily variations of the ground magnetic data for case 1 (left), as well as a map of the stations and the LEO orbit (right)

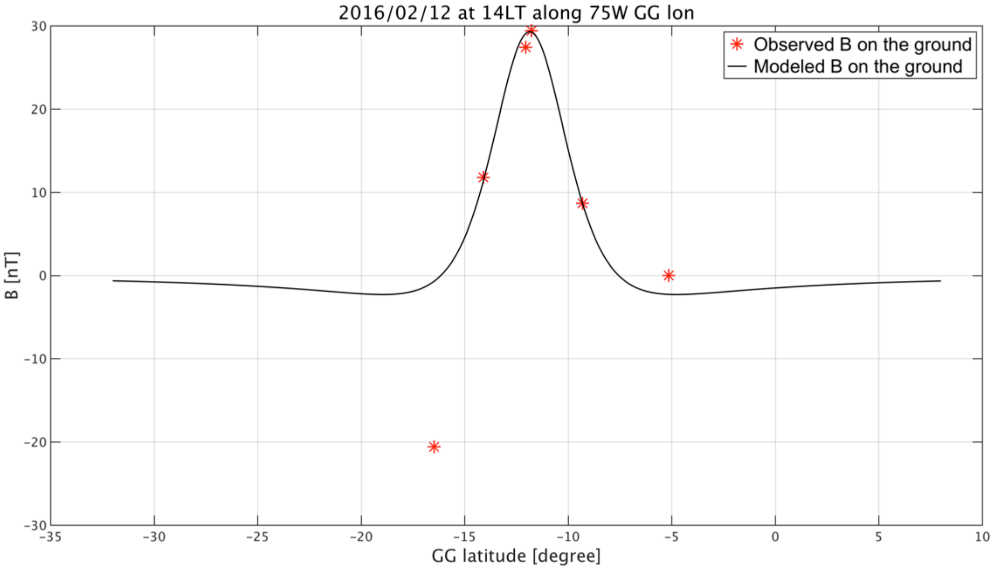

Figure 3.4 Latitudinal profiles of the model values (black solid line) and the observed values (red star) of the EEJ-oriented magnetic field for case 1

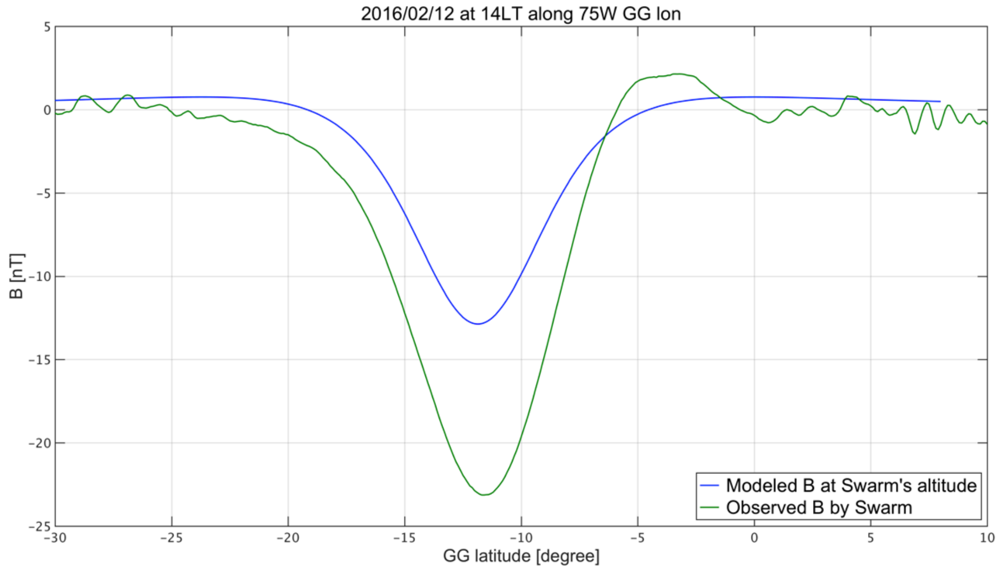

Figure 3.5 Latitudinal profile of the modeled field for the LEO altitude (blue) and the observed LEO magnetic data for case 1

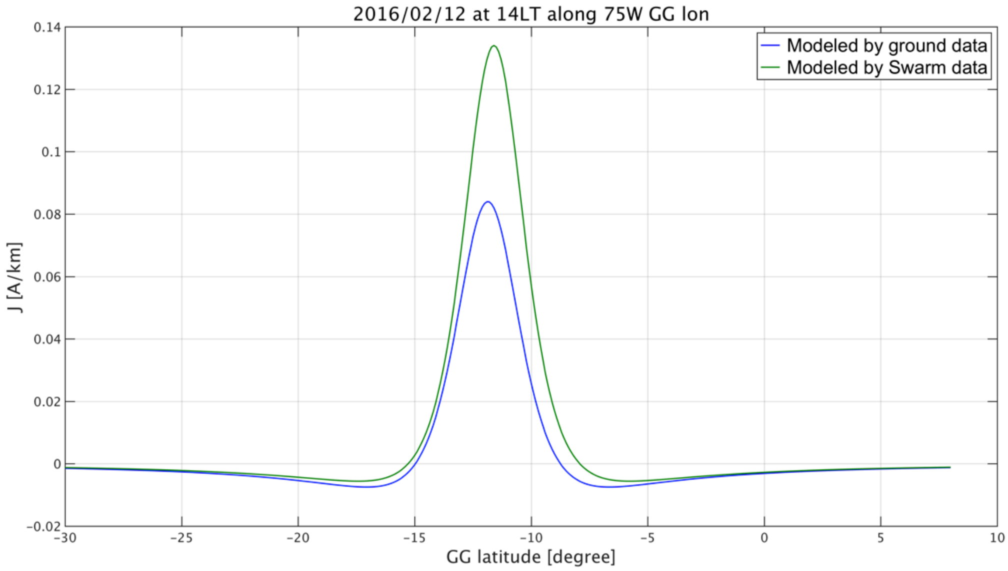

Figure 3.6 Latitudinal profile of the estimated EEJ current structure from ground magnetic data (blue) and LEO magnetic data (green) for case 1

3.2.2 Case 2: March 1, 2016 at 12 p.m. LT

The LT variation of the northward component of a 1-hour magnetic field on the ground for this case study as well as the location information of the ground magnetic data and the Swarm data are illustrated in figure 3.7. The format of the figure is same as that of figure 3.3 except that the data in the figure are from March 1, 2016. The modeled field and the observed field for this case are compared in figure 3.8 in order to confirm whether the modeled field explains or fits the observed values well. The format of this figure is same as that of figure 3.4. In essence, the modeled field corresponds well to the observed-field data points, and therefore, a flow of additional local current is not observed in this case. Figure 3.9 (Figure 3.10) shows the comparison between the estimation of the field (current density) from ground-based data and Swarm-data, just as was shown in figure 3.5 (figure 3.6). The peak amplitudes of both fields are almost comparable, that is, a 1 to 2 nT difference between them is observed. However, the position of the EEJ axis for the ground-based data is shifted southward of the one for the Swarm-based data, i.e. there is a shift from -12.03 degrees of latitude to -11.50 degrees of latitude, respectively. This shift is due to the difficulty involved in determining the zero level of the EEJ-related field, where the mean value from each station during nighttime (6 p.m. to 6 a.m. LT) was used in this study. Another possibility is that local currents could be affecting the profile, that is, decreasing the value obtained at ANC. In addition, it is possible that the peak value was detected at HUA and not at ANC. The estimated current structure from ground magnetic data and Swarm data are shown in figure 3.10. Similarly, the estimated current from the ground data shifts southward of the one estimated from the Swarm data. The peak current densities for the ground-based and Swarm-based estimates were 0.106 A m^{-2} and 0.097 A m^{-2} respectively. The widths for the ground-based and Swarm-based estimates were determined as 5.22 degrees of latitude and 4.29 degrees of latitude, respectively. In short, the estimated peak current densities were comparable but a larger amplitude and a southward shift were observed for the estimate from ground-based data when compared to the Swarm-based data.

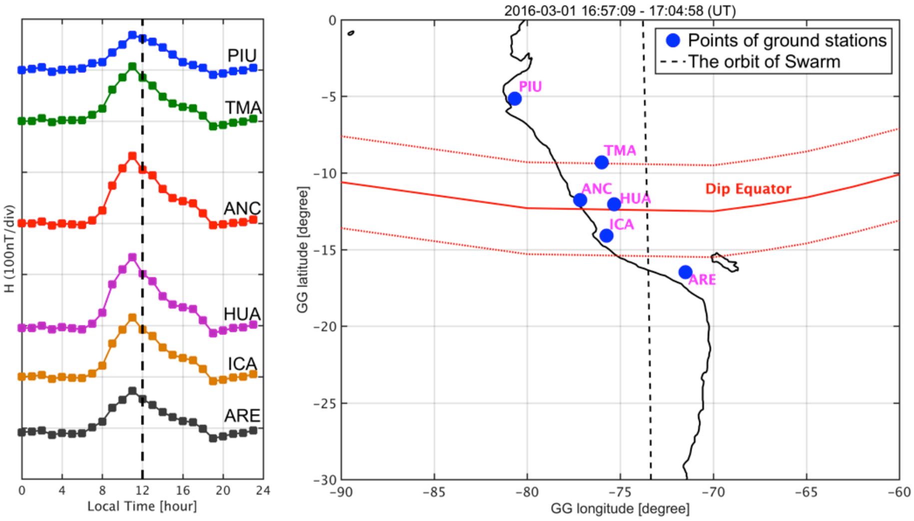

Figure 3.7 Same as in figure 3.3, but for case 2

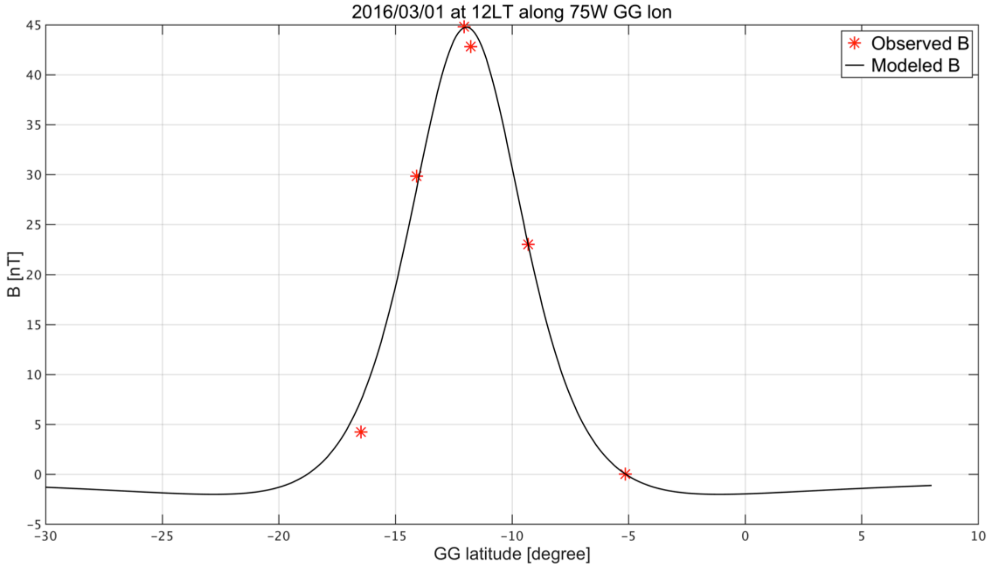

Figure 3.8 Same as in figure 3.4, but for case 2

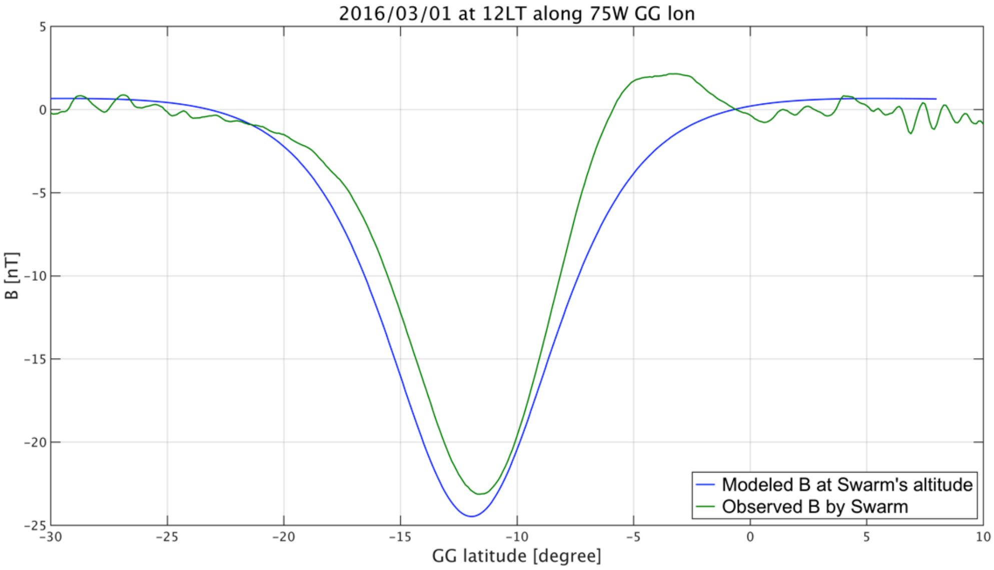

Figure 3.9 Same as in figure 3.5, but for case 2

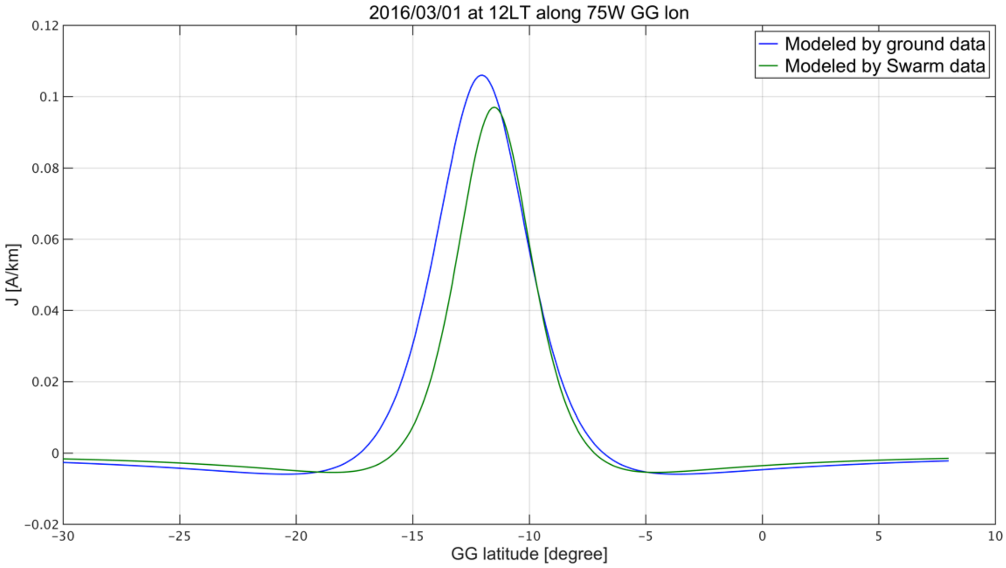

Figure 3.10 Same as in figure 3.6, but for case 2

3.2.3 Statistical results of the comparison

The average modeled fields and current structures at different LTs for both the ground-based data and Swarm-based data were derived. The events are as summarized in Table 3.1. The minimum number of events, which occurred between 8 a.m. and 10 a.m. LT, was two, while the maximum number of events was six at 3 p.m. LT. The modeled fields at different LTs are shown in figure 3.11, where a blue-colored (green-colored) plot indicates the modeled magnetic field produced by the EEJ, estimated from ground-based (Swarm-satellite-based) magnetic data. As shown in the figure, the fields match each other well at 9 a.m., 10 a.m., 11 a.m., and 3 p.m. LT. In contrast, the modeled field from ground magnetic data shows larger amplitudes at 8 a.m. and 12 p.m. LT while smaller amplitudes are observed at 1 p.m. and 2 p.m. LT compared with the field estimated from Swarm data. Moreover, a field caused by a return current of the EEJ is only observed in the ground-based model and at 1 p.m. and 2 p.m. LT, which is at around -18 or -6 degrees of geographic latitude. Figure 3.12 shows the EEJ current structures estimated from the ground magnetic data and the Swarm data, which are denoted by blue and green lines, respectively. Although the current structures show good correspondence at 9 a.m., 10 a.m., and 11 a.m. LT, a smaller amplitude of the peak current density for the ground-based data was estimated at 1 p.m. and 2 p.m. LT. Meanwhile, a larger amplitude for the ground-based data was estimated at 12 p.m. LT. Most of the characteristics observed in this figure comparing current structure were the same as the one comparing the modeled fields, for example, a southward-shifted and larger amplitude for the ground-based data at 12 p.m. LT. However, the narrower current flow observed at 8 a.m., 1 p.m., 2 p.m., and 3 p.m. LT in the ground-based model, is difficult to observe for the modeled magnetic field comparisons (figure 3.11). Since such sharp currents were also detected by the Swarm data at 2 p.m. and 3 p.m. LT, these currents are not an error in the ground magnetic data. It should also be noted that the smaller amplitude of these sharp or narrower currents for Swarm data is probably due to the different distances from the current, which are around 110 km for the ground data and more than 300 km for the Swarm data. The large discrepancy between them at 4 p.m. LT is probably due to the difficulties in removing the Sq-related field from the raw data since the equatorial enhancement of the field becomes smaller around dusk and dawn. Table 3.2 summarizes the averaged parameters for the EEJ structure, where the values for the ground-based and Swarm-based estimates are the top and bottom values in each cell, respectively. As already mentioned above, the parameters of the EEJ in the table, that is, J_0, w, Y_0 are comparable for the ground-based and Swarm-based estimates at 9 a.m., 10 a.m., and 11 a.m. LT, and they are less than ten percent apart. On the other hand, different values for the peak current density were estimated at all other LTs, which were sometimes more than twice the values apart. The reason for this is probably owing to the already-mentioned difficulties in removing the Sq-based variations. Another possibility is that the assumption for the altitude of the modeled EEJ is incorrect. Note that the altitude of 110 km from the ground was assumed in this study. In addition, the larger width of the EEJ estimated from the Swarm data at 4 p.m. LT is also possibly due to the Sq-removal since the Sq variation for the Swarm data was derived from spline interpolation between the off dip equators at ±12° away from the EEJ axis.

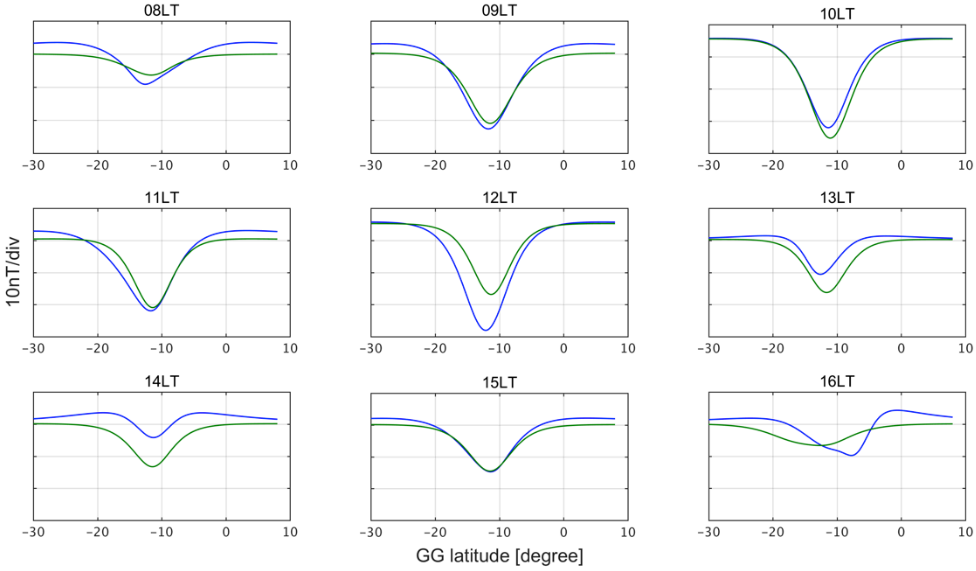

Figure 3.11 Comparison between modeled fields obtained from ground magnetic data (blue) and Swarm magnetic data (green)

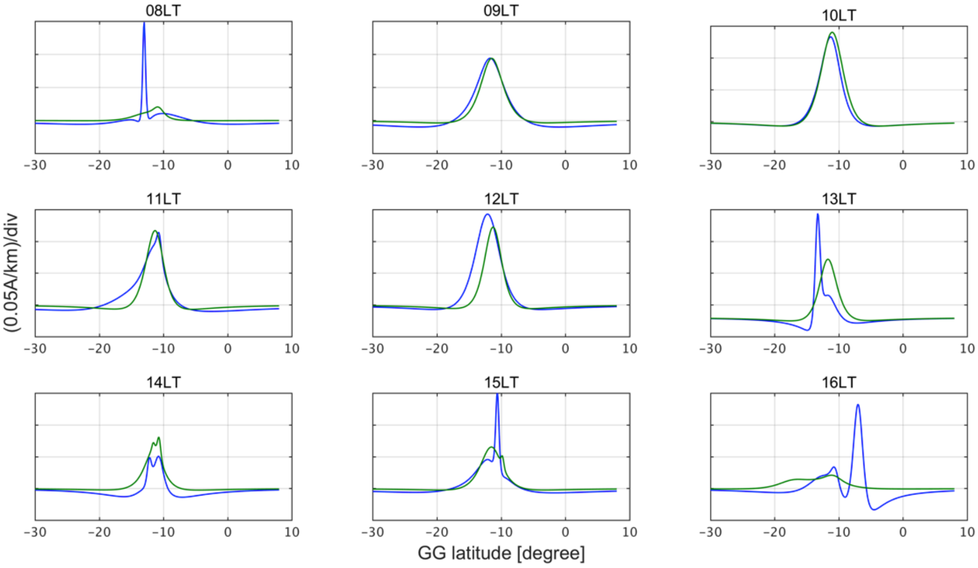

Figure 3.12 Comparison between the estimated current structure from ground magnetic data (blue) and Swarm magnetic data (green)

LT	J_0 [A km^{-2}]	α	a	w [km]	Y_0 [degrees]
08	229 ± 189 36 ± 5	-1.55 ± 0.85 -0.30 ± 0.20	520 ± 470 325 ± 155	349 ± 290 608 ± 71	-11.6 ± 0.9 -11.8 ± 1.0
09	95 ± 22 96 ± 14	-0.98 ± 0.61 -0.50 ± 0.07	578 ± 259 410 ± 77	588 ± 79 578 ± 90	-10.4 ± 0.1 -11.4 ± 0.3
10	135 ± 11 141 ± 9	-0.60 ± 0.10 -0.55 ± 0.05	380 ± 90 390 ± 30	486 ± 76 526 ± 17	-11.4 ± 0.3 -11.1 ± 0.2
11	132 ± 16 120 ± 30	-0.85 ± 0.40 -0.63 ± 0.04	418 ± 318 327 ± 47	433 ± 260 417 ± 71	-12.4 ± 1.0 -11.5 ± 0.3
12	143 ± 27 123 ± 30	-0.57 ± 0.05 -0.53 ± 0.09	433 ± 39 313 ± 40	575 ± 29 433 ± 51	-12.1 ± 0.1 -11.3 ± 0.2
13	197 ± 165 93 ± 26	-1.00 ± 0.49 -0.67 ± 0.31	230 ± 114 320 ± 51	249 ± 116 421 ± 117	-11.7 ± 0.7 -11.6 ± 0.2
14	85 ± 20 103 ± 35	-2.34 ± 2.04 -0.50 ± 0.11	264 ± 135 244 ± 175	249 ± 155 340 ± 243	-11.2 ± 0.5 -11.4 ± 0.4
15	161 ± 197 82 ± 30	-1.08 ± 0.45 -0.57 ± 0.21	555 ± 339 343 ± 146	534 ± 251 495 ± 220	-11.9 ± 0.9 -11.2 ± 0.7
16	196 ± 143 32 ± 1	-1.03 ± 0.33 -0.37 ± 0.17	287 ± 180 503 ± 193	302 ± 213 824 ± 145	-10.3 ± 2.1 -13.5 ± 2.7

Table 3.2 Averaged parameters of the EEJ structure derived from ground magnetic data (top value in each cell), and LEO magnetic data (bottom value in each cell) at different LTs

3.3 Discussion

As mentioned in the previous section, the differences in the modeled field or estimated current structure may result from the assumption of the altitude of the EEJ, the local current effect or the Sq removal. Accordingly, these effects were investigated. At first, the effect of local current, which is assumed to be induced current here, was investigated. Figure 3.13 reveals the latitudinal profile of the modeled horizontal component of the field represented by a blue solid line. The modeled field with the effect of the induced field is indicated by the blue broken line. In addition, red dots correspond to the extracted EEJ variation observed at each station. In this figure, it was assumed that the induced current flowed eastward at a certain latitude in the sea, that is, 100 km southward of the ARE station (at around -18 to -17 degrees of geographic latitude) and below 50 km sea level. The ribbon current of constant intensity model was assumed for the induced current. As seen in figure 3.13, the large depression can be explained by the field produced by the induced current under the sea. Figure 3.14 shows the latitudinal profiles of the EEJ variation in the vertical component, where the modeled field, the modeled field with the induced field and the observed field data are denoted by a blue solid line, a blue broken line and red dots, respectively. The good correspondence between the modeled field with the induced field and the observed field data may indicate the existence of a local current. Note that only one station exists in the area where induced currents flow, therefore more data stations are necessary in order to study the details of this induced current. In reality, it is unlikely that the induced field was present for case 2 on March 1, 2016 as seen in the figure 3.8. For the Swarm observation, however, the return current, which is a well-known EEJ structure in LEO measurements (e.g. *Luhr et al.*, (2004); *Jadhav et al.,* 2002; *Onwumechili*, 1967), can be seen only northward of the dip equator. Adding an induced field represents the return current southward of the dip equator as well, possibly indicating the existence of an induced current in the sea near the ARE station. The smaller amplitude of the ground-based estimation of the EEJ variation than the Swarm-observed variation might indicate that the altitude of the EEJ was not constant, where 110 km was assumed. In order to confirm how different assumptions of the altitude affect the results, the relationship between the altitude, the peak current density, and the width of the EEJ were studied. The results are as follows:

$$J_0 = 0.628\,alt\ + 16.007 \qquad (3-1)$$

$$w = -1.344\,alt\ + 498.191 \qquad (3-2)$$

where J_0 is the peak current density and its unit is A m^{-2}, alt is the altitude and w is the width of the EEJ, for which both units are km. As both equations show, a higher altitude results in a larger estimated peak current density or a smaller estimated width of the EEJ. Therefore, a possible reason for smaller (larger) field or current density estimates from ground data is the assumption of a lower (higher) altitude of the EEJ. For example, figure 3.16 shows the difference between the latitudinal distribution of the field at the altitude of the Swarm satellite and the Swarm-observed magnetic data. The original model field obtained for the EEJ altitude of 110 km estimated a smaller variation compared to the observed variation, whereas the model field obtained for the EEJ altitude of 195 km estimated a variation of almost comparable amplitude to the observed field although it was a narrower distribution than the observed field. It should be noted that the conductivity is inefficient at 195 km altitude as shown in figure 3.17, in which the height profiles of Pedersen conductivity (blue line), Hall conductivity (green line), Cowling conductivity (red line) and Parallel conductivity (black line) are shown. Additionally, the studies of rocket measurements revealed the altitudinal extent of the EEJ was between 89 and 136 km (*Maynard and Cahill*, 1962), and the altitude of 195 km is inconsistent with that region. Therefore, according to equation (3-1) and equation (3-2), the different peak current densities and widths of the EEJ of +0.20 A m^{-2} and +25 km, respectively may be the result of changes in the altitude. Since most of the previous studies on the EEJ structure focused on the general characteristics of the EEJ, i.e., magnetic data around noon-time was adapted, the comparison of this study with previous studies should also be performed at 12 p.m. LT. For the current density, *Luhr et al.*, (2004) revealed that the average current density was about 0.15 A m^{-2} while *Jadhav et al.,* (2002) revealed it to be about 0.20 A m^{-2}. The results from this study showed 0.14 A m^{-2} for the ground-based estimation and 0.11 A m^{-2} for the Swarm-based estimation. The former result is consistent with the result of *Luhr et al.*, (2004). As for the width of the EEJ, *Onwumechili and Ezema*, (1992) analyzed POGO satellite data and found the width of the EEJ to be around 2.8 degrees for all longitudes with a very small standard deviation. On the other hand, the results from this study for the ground-based and Swarm-based estimates revealed 3.7 and 3.2 degrees of latitude, respectively. The reason for the ground-based estimation being larger can be explained by equation (3-2). According to this equation, a higher altitude, which alternatively means that the measurements exist at further distances, results in a narrower EEJ. Therefore, it can be said that the ground-based estimation tends to have a larger width than the satellite-based estimation.

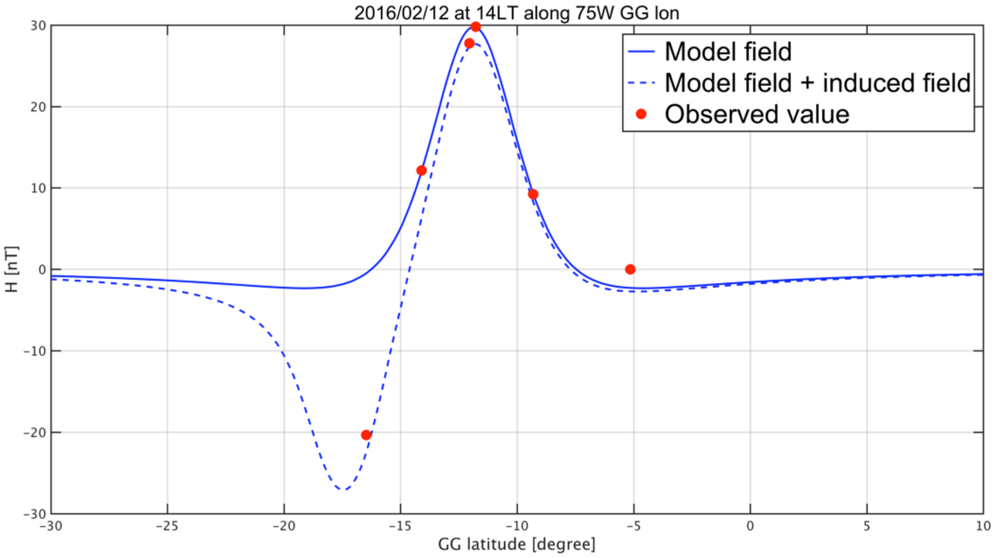

Figure 3.13 Latitudinal profiles of the model field (blue solid line), the model field including an induced current effect (blue broken line) and the observed field data (red dots) all for the horizontal component

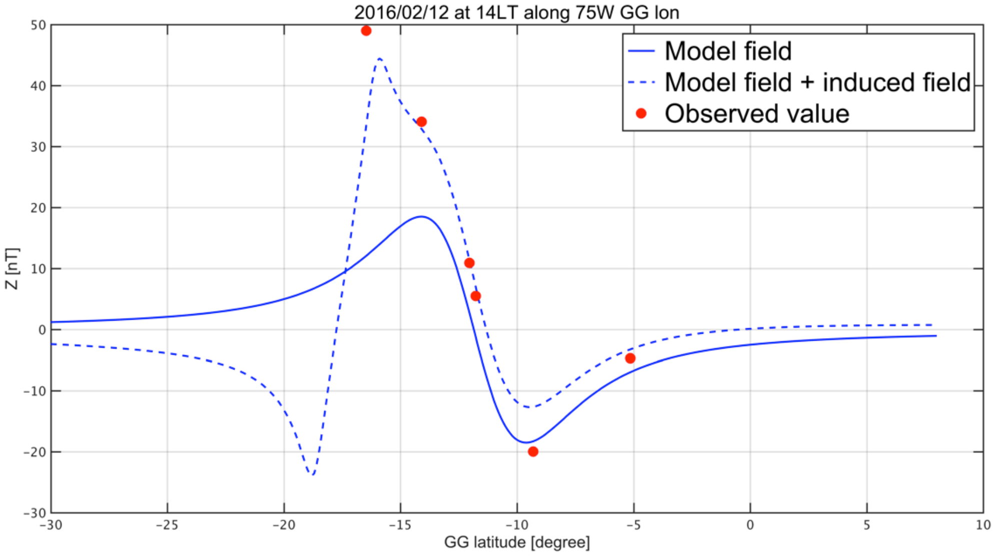

Figure 3.14 Latitudinal profiles of the model field (blue solid line), the model field including an induced current effect (blue broken line) and the observed field data (red dots) for the vertical component

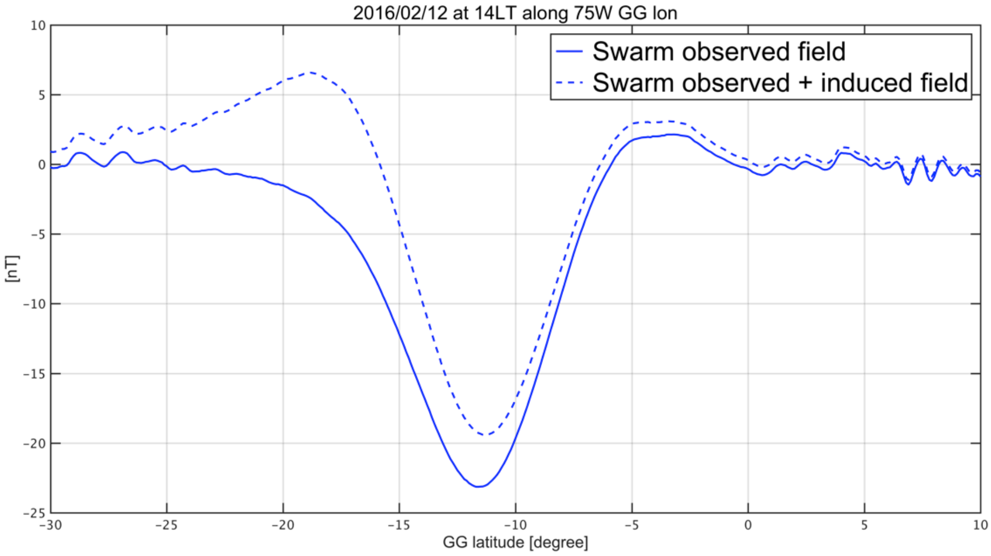

Figure 3.15 The observed EEJ field from the Swarm satellite and the field which includes the induced current effect

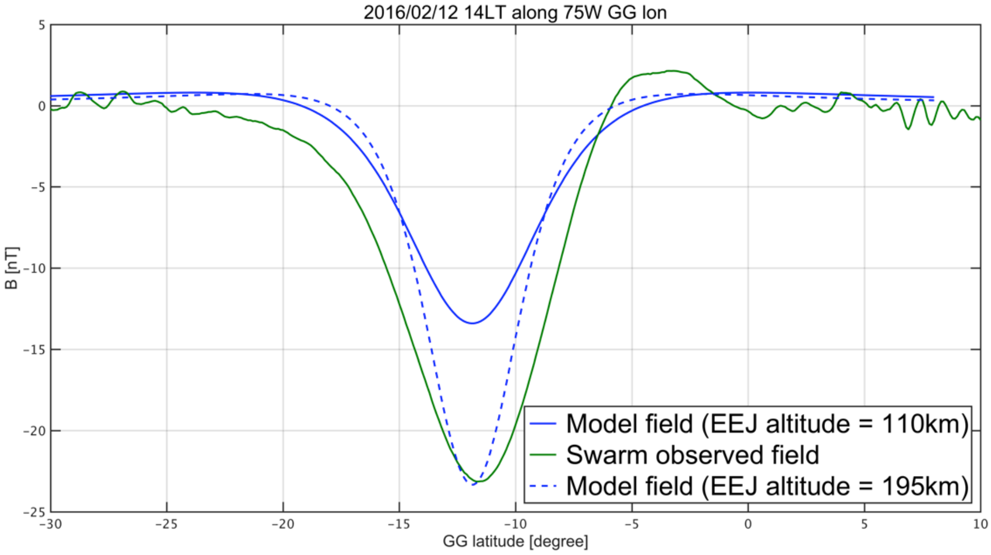

Figure 3.16 Latitudinal variation of the EEJ field observed by the Swarm satellite (green solid line), the model field under the assumption of 110 km altitude of the EEJ (blue solid line) and the model field for a 195 km altitude of the EEJ (blue broken line)

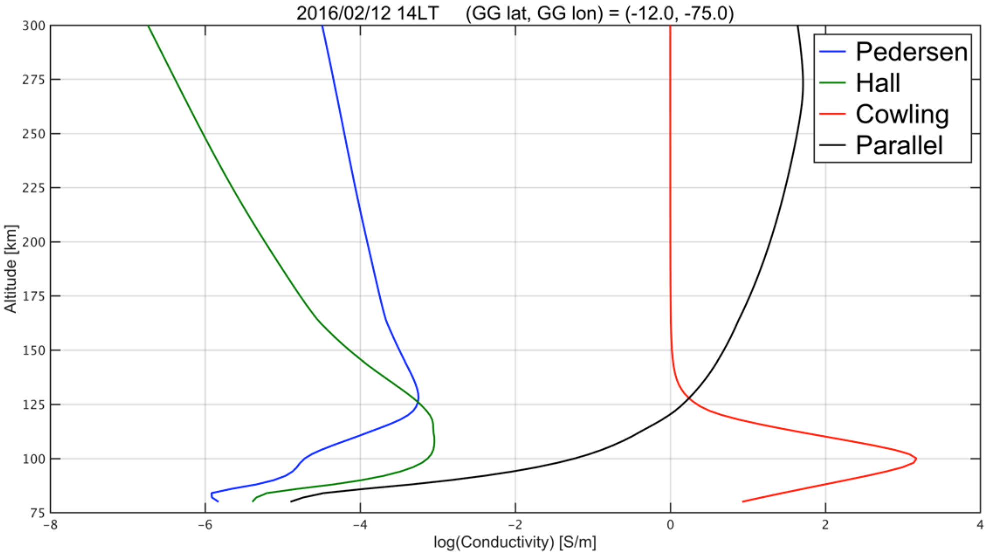

Figure 3.17 The height profile of the ionospheric conductivities, where the blue-, green-, red- and black-colored plots correspond to Pedersen conductivity, Hall conductivity, Cowling conductivity and Parallel conductivity, respectively, at 12 p.m. LT on February 12, 2016. The location is given by (-12.0, -75.0) degrees of geographic latitude and longitude

4. Long term variation of the EEJ structure

In order to investigate the long-term variation of the equatorial enhancement of the daily variation, the EEJ current structure was estimated using the model developed in this study. Subsequently, the long-term variation of each parameter and its correlation with F10.7, which is an index to evaluate the strength of ionization in the ionosphere, are obtained in order to investigate which parameters are controlled by F10.7.

4.1 Methodology and dataset

The method used to derive the EEJ structure was essentially the same as that shown in Chapter 3. The equatorial enhancement component was derived by subtracting the magnetic field observed at PIU, which was used as the reference station for Sq variation. Then, the value for the equatorial enhancement at 12 p.m. LT was adopted as the magnetic field for daily variation. Using the method of least squares between this value and that obtained from equation (2-2), the daily sets of parameters for the EEJ structure were estimated. The magnetic data used in this study were obtained between January 1 and December 31,2016. The dates whose available data were from less than four stations or the unavailable data at PIU were removed from the dataset. In total, 200 days in the year were selected for this study.

4.2 Results and discussions

Figure 4.1, in order from top to the bottom shows the day-to-day fluctuations of the EEJ variation, the estimated peak current density, the full width of the EEJ current, and the position of the EEJ axis in 2016. In the top panel, semiannual variation can be seen where a maximum is observed around April while a minimum is observed around June. This trend is one of the well-known EEJ features (*Stening* (1995a)). The peak current density, as shown in the second panel from the top, also reveals a similar trend to the EEJ variation. In contrast, both the width and the position of the EEJ center did not show semiannual variation. The width from January to May was, however, smaller than the width from May to November. As for the position of the EEJ axis, the value was fixed around -12 degrees of geographic latitude except from the end of March to the end of April. As shown in figure 4.2, a linear relationship exists between the EEJ variation at HUA and the peak current density. The high correlation coefficient, that is, r =0.75 means that the semiannual trend in the EEJ variation observed by ground magnetic data is as a result of the current density. On the other hand, both the width and the position of the EEJ center do not show a linear relationship with the EEJ variation as shown in figure 4.3 and figure 4.4. Note that the magnetic data used here were taken at Huancayo, which is just below the EEJ axis, and therefore it is probable that other EEJ structural changes, such as the change of width, do not affect the field substantially at that location. However, an interesting feature can be seen for both of the relationships between EEJ variation and the width/the positioning of the EEJ axis Regarding the width, a higher amplitude of the EEJ variation tends to result in a narrower EEJ. Concerning the position of the EEJ axis, a higher amplitude of the EEJ variation contributes to the particular positioning of the EEJ axis. In other words, the deviation becomes smaller. This kind of trend was reported by *Onwumechili and Agu,* (1981b) and *Jadhav et al.*, (2002) while *Luhr et al.*, (2004) reported the inverse trend, which is that a higher amplitude of the current density corresponds to a larger width of the EEJ. The former authors suggest that the current intensity is conserved and larger/narrower EEJ tends to be lower/higher current density, whereas the latter authors suggest that the longitudes with larger cross-sections of the Cowling channel larger currents supposed to flow. Another possibility is due to the disappearance or depression of the EEJ when the EEJ variation is small; therefore, the EEJ variation might include some of the Sq-related field. Figure 4.5 shows a scatter plot of F10.7 versus the EEJ structural parameters and the EEJ variation on the ground. The top left panel shows the scatter with the EEJ variation on the ground while the top right panel shows the scatter with the peak current density. The bottom left panel shows the scatter with the width of the EEJ meanwhile the bottom right panel shows the scatter with the position of the EEJ axis. As can also be seen from the figure, the poor correlation between the F10.7 and the EEJ parameters was revealed. All of the correlation coefficients were almost zero. Since *Yamazaki et al.*, (2010) and *Hamid et al.*, (2013) reported positive correlation between the EEJ variation and F10.7 with correlation coefficients of 0.53 and 0.43, a positive correlation was also expected with the estimated current density. It should be noted that a poor correlation of F10.7 with the EEJ variation at HUA was found in this study. A possible explanation for this poor correlation is that the F10.7 was not very strong in 2016, and did not play an important role in atmospheric tides. As suggested by *Liu et al.*, (2006), the density in the ionosphere is not solely attributed to EUV radiation but atmospheric dynamics must also be considered. Therefore, the comparison of the EEJ parameters with atmospheric effects is encouraged for future work.

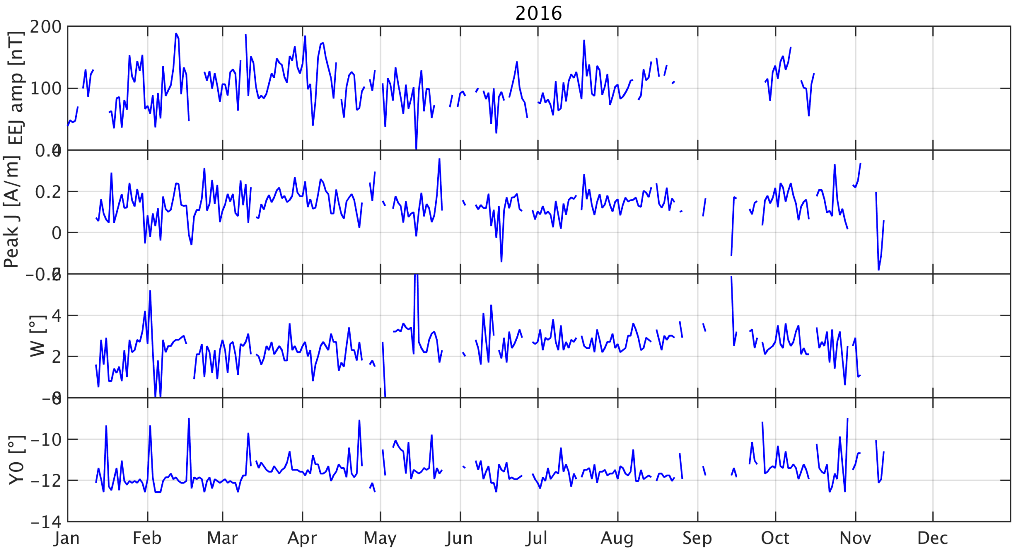

Figure 4.1 Long-term variations of the EEJ structural parameters. In order from the top to bottom: the observed equatorial enhancement of the field at HUA, the peak amplitude of the EEJ current, the width of the EEJ and the position of the EEJ axis

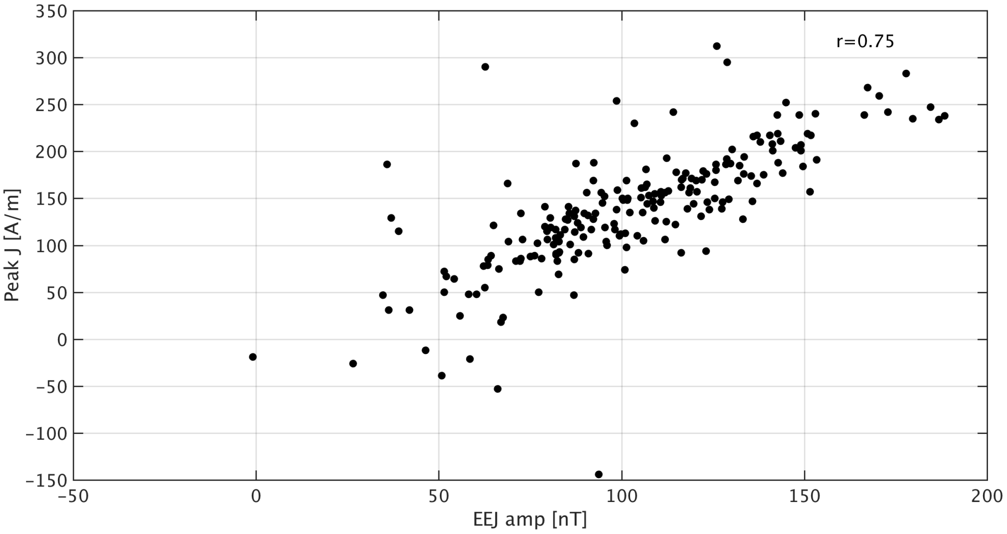

Figure 4.2 The scatter plot of the equatorial enhancement versus the peak amplitude of the EEJ current

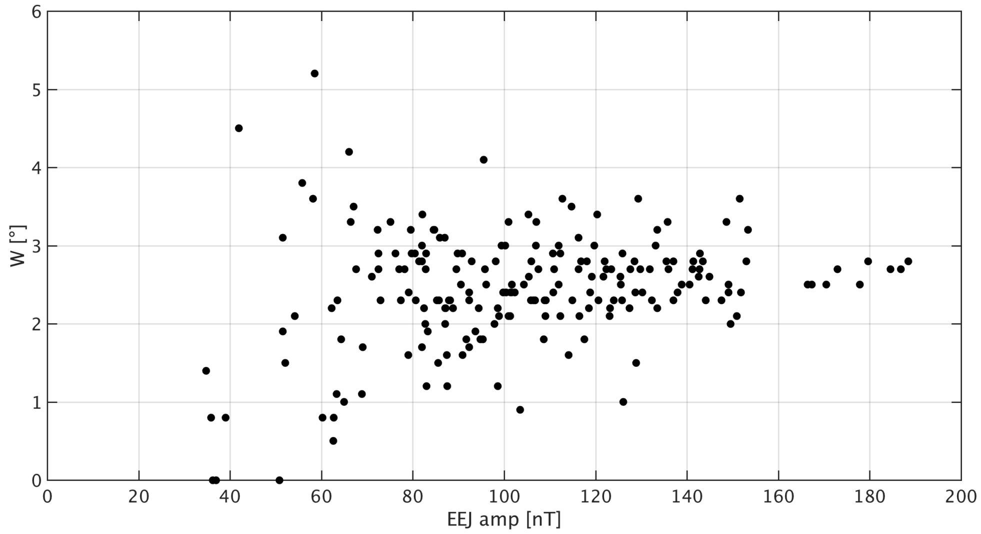

Figure 4.3 The scatter plot of the equatorial enhancement versus the width of the EEJ current

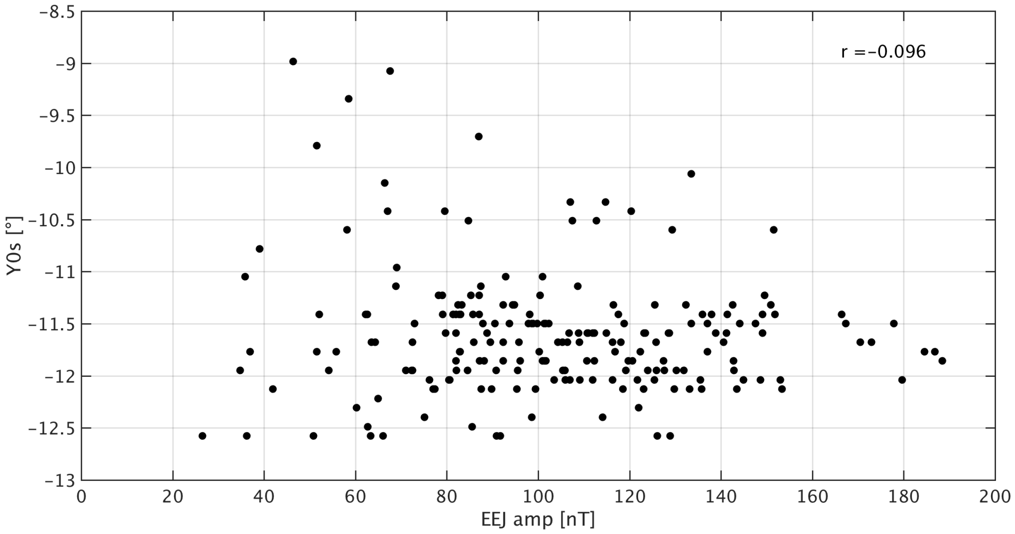

Figure 4.4 The scatter plot of the equatorial enhancement versus the position of the EEJ axis

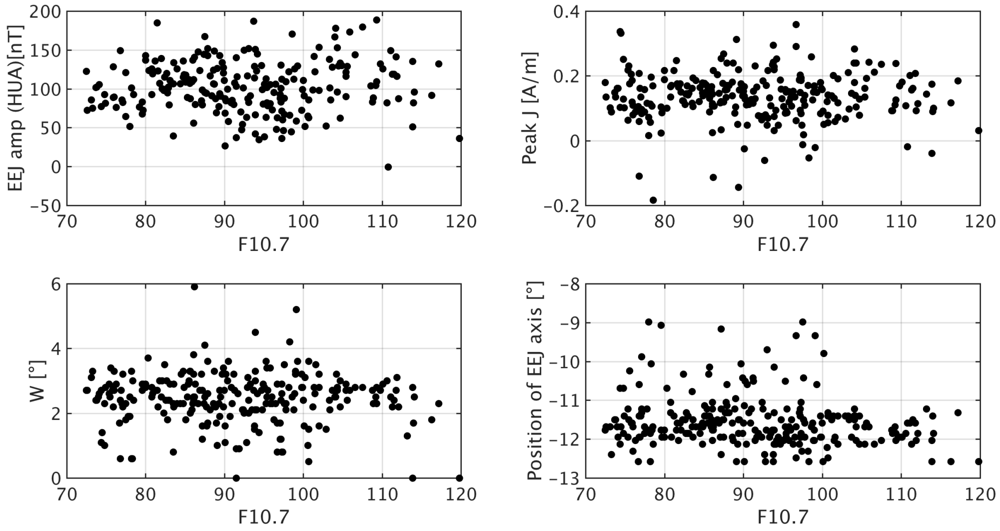

Figure 4.5 Scatter plot of F10.7 versus the equatorial enhancement (top left), the peak amplitude of the EEJ current (top right), the width of the EEJ (bottom left) and the position of the EEJ axis (bottom right)

5. Temporal variation of the EEJ structure

In this chapter, the temporal variation of the EEJ structure will be introduced through some case studies during normal equatorial electrojet, counter electrojet, and geomagnetically active times. Each event was determined by carefully checking the observation for the EEJ, the Counter ElectroJet (CEJ) and the Dst index for a storm event. The continuous distribution current density model as the EEJ current was applied just as shown in previous chapters.

5.1.1 The EEJ current structure during a quiet time and with a normal EEJ

Beginning from the LT structure of the normal EEJ means that there is no full-CEJ in a day. As a case study, the date of July 21, 2016 was chosen on which the daily-average Kp index was 1.25. The hourly-average variations of the horizontal component (vertical component) are shown in the top left (top right) panel of figure 5.1. The variations from top to bottom correspond to the observatories from north to south, and the dip equator in this region is located near ANC and HUA. It can be seen from the figure that the peak of the daily variations at each station was at 11 a.m. LT, and the largest peak value was obtained at HUA. On the other hand, for the Z component, the peak value exists between 11 a.m. and 1 p.m. LT, and the maximum/minimum of its peak values can be seen at NAZ/TMA, respectively. Additionally, the LT dependence of the equatorial enhancement was derived by subtracting the variation at PIU, which was used as the reference station for the Sq field, and is shown in the bottom panel of figure 5.1. The LT distribution was almost same as the variation before the subtraction except for the negative variation that could be seen at ARE after 12 p.m. LT and at NAZ after 3 p.m. LT. Figure 5.2 illustrates the LT distribution of the estimated EEJ structure for this day. In the figure, the x-axis and y-axis correspond to the LT in Peru and the geographic latitude, respectively, and the color of the contours represent the current density (A/m^{-2}). It can be seen that the EEJ is well confined to a certain latitude (~ -12 degrees of latitude) and rises to its peak around 11 a.m. LT, then disappears around 5 p.m. LT. Another characteristic of the EEJ was revealed that the confinement of the EEJ became remarkable after 9 a.m. LT. This feature can also be seen for the magnetic data in figure 5.1 as rapid increases of the field at HUA and ANC compared with the other stations. As for the return current of the EEJ, its minimum current density can be seen at 1 p.m. LT around -18 and -5 degrees of latitude, that is, approximately 5 to 6 degree away from the EEJ axis. It should be noted, however, that a symmetric structure of the current density according to the EEJ axis was assumed here. Moreover, the position of the center of the return current moved towards the equator or extended near the dip equator. This feature also can be seen for the magnetic field on the ground in the figure 5.1 since the equatorial enhancement at NAZ with latitude that is northwards of ARE also became negative but at a later time than ARE. The minimum/maximum value of the return current/EEJ were -0.04 A/m^{-2} and 0.22 A/m^{-2} at $GG\ lat = -4.83°$ and $GG\ lat = -11.59°$, respectively.

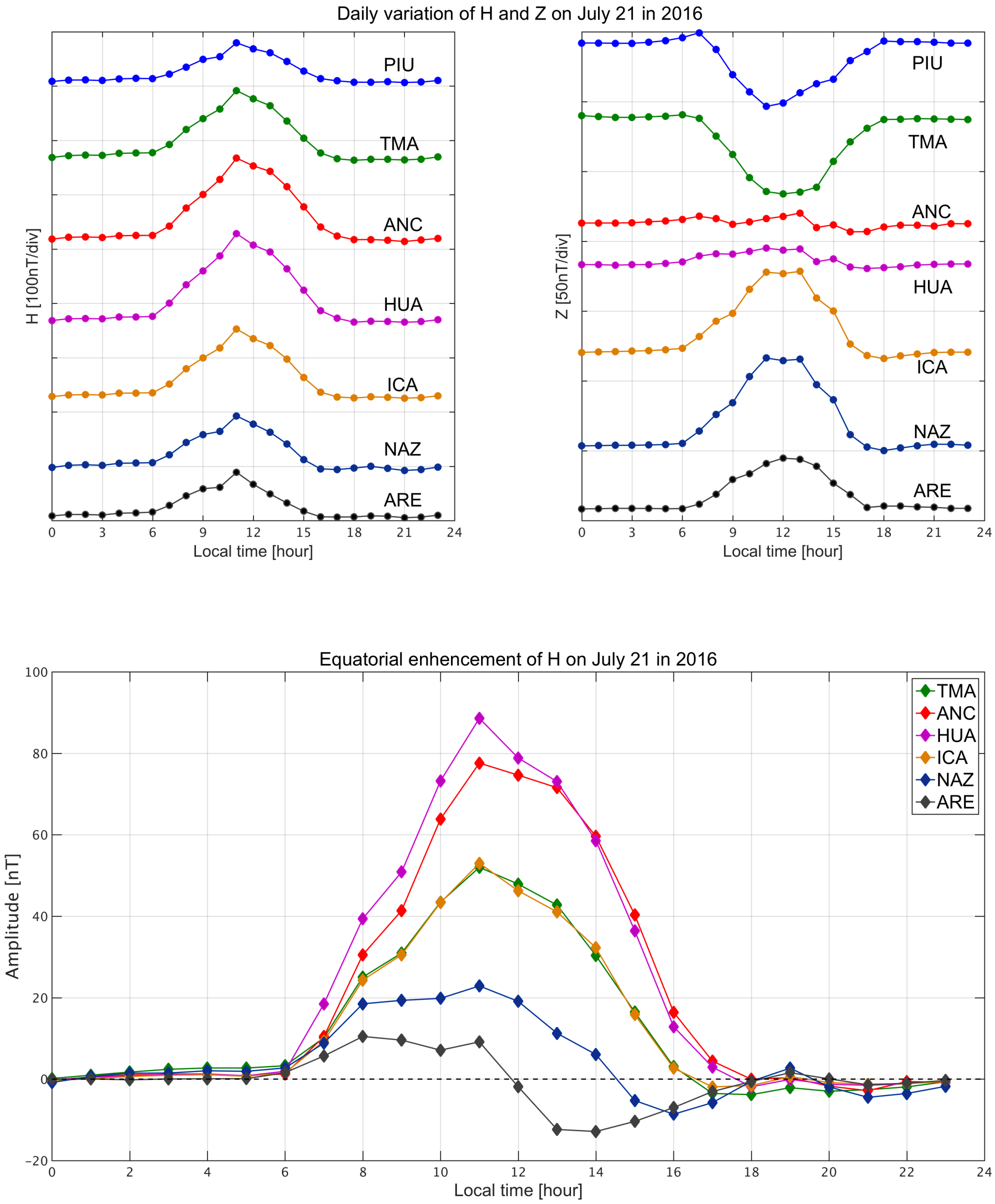

Figure 5.1 Daily variation of the horizontal component of the magnetic field on July 21, 2016 during a geomagnetically quiet time (top left). Same as in (top left) but for the vertical component (top right) and The equatorial enhancement of the daily variation derived by subtracting the variation at PIU, which is used as the reference station of Sq variation (bottom)

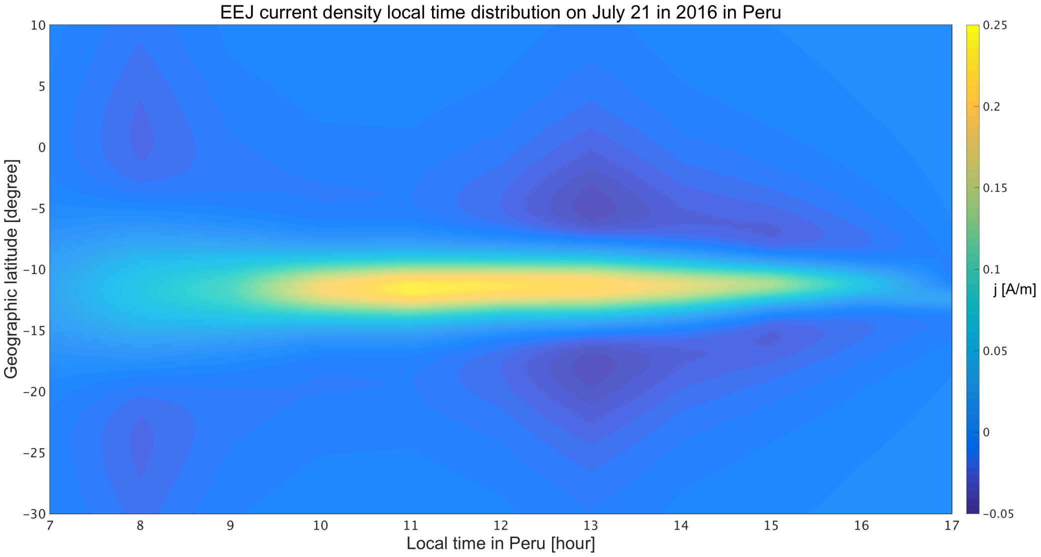

Figure 5.2 An EEJ current density distribution in LT-GG latitude flame on July 21, 2016

5.1.2 The EEJ current structure during a quiet time but with a CEJ in the morning

Figure 5.3 shows the daily variation of the horizontal component and the vertical component in the top panels while the bottom panel shows the equatorial enhancement as in figure 5.1 but for October 11, 2016. On this day, the CEJ was observed near the dip equator in morning, which can be seen as the negative variation of the H component at entire latitude and negative (positive) variation of the Z component at southward (northward) of the CEJ axis. Therefore, the CEJ for this case exists around HUA or ANC since the Z component at 7 a.m. LT turned from negative to positive between ICA and TMA. The existence of the CEJ became clear when the equatorial enhancements were extracted as shown in figure 5.3(c). The minimum value at ANC at 7 a.m. LT indicates that the CEJ axis exists near ANC. The trend of the LT distribution of the equatorial enhancement for this CEJ event is almost the same as the one for the normal EEJ event discussed in the previous section, while the maximum amplitude at HUA at 11 a.m. LT for the CEJ events was approximately half of the normal EEJ event. Moreover, the distribution at ARE also shows some different features to the normal EEJ event, since it became positive again after 1 p.m. LT even though it was negative at 12 p.m. LT. Figure 5.4 illustrates the local time distribution of the estimated local time current structure for this CEJ event. The CEJ structure at 7 a.m. LT seems to be almost identical to the one for the EEJ although the direction of current is westward. The position of the CEJ axis existed around -12 degrees of latitude and its width was approximately 3 degrees of latitude. Different features compared with normal EEJ day were that little return current flows at the flanks of EEJ in entire LT. In addition to that, the widths of the midday EEJ for this event became smaller around noon as the variation at ARE depressed around noon, which probably indicates that this area was no longer found within the EEJ band. The average and peak current densities were roughly half of those of the normal EEJ. Note that it is well known that there is day-to-day variability in the EEJ, and hence it is not possible to conclude that the smaller current density was due to the appearance of the CEJ. This will be discussed in later sections.

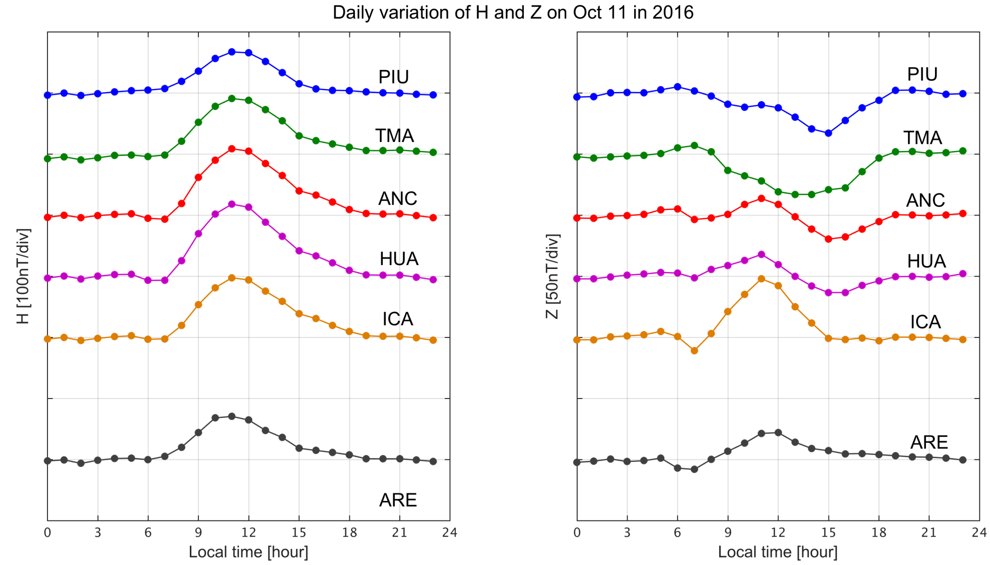

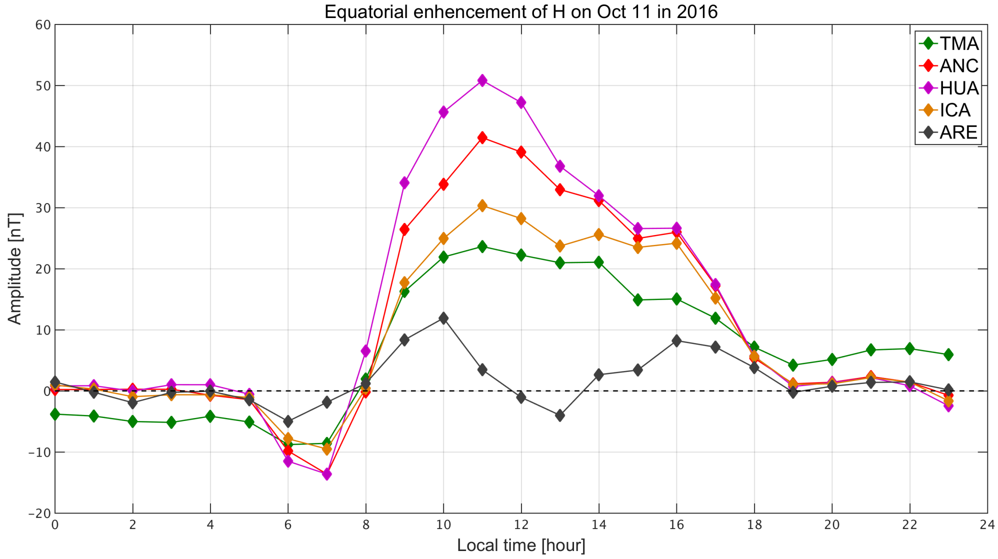

Figure 5.3 Same as in figure 5.1 except that the data is for October 11, 2016 when the CEJ was observed in morning

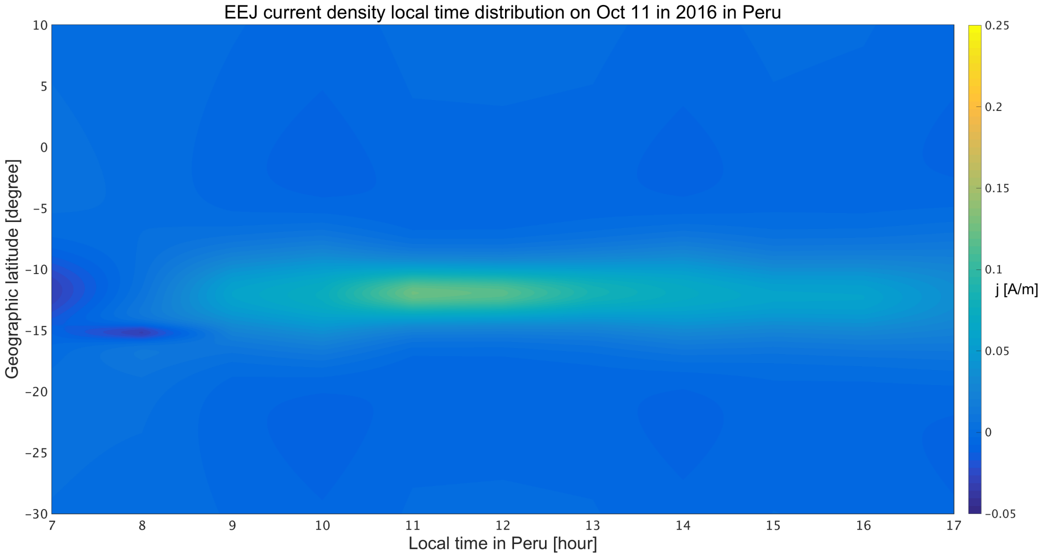

Figure 5.4 Same as in figure 5.2 but for the data from October 11, 2016

5.1.3 The EEJ current structure during a storm time

In order to examine the relationship between the time developments of the EEJ current structure during a storm time, the day was divided into three stages as can be seen in figure 5.5. The timings of the stages were determined by a change of date in a LT frame, and t_0 corresponds to the start time of the day before the storm occurred. The variables t_1 and t_2 correspond to the start time of the days during which the main phase and the recovery phase occurred. They are indicated in figure 5.5 by black solid vertical lines with the time series of the Dst index. Figure 5.6 and figure 5.7 display the magnetic field change and the EEJ current structure for the stage between t_0 and t_1 and are presented in the same manner as figure 5.1 and figure 5.2. Figures 5.8 and 5.9 and figures 5.10 and 5.11 display the same information but for the stages between t_1 and t_2 and between t_2 and t_3, respectively. The equatorial enhancement of the magnetic field between t_0 and t_1, which is shown in figure 5.6(c), has an anomalous feature compared to the case of the normal EEJ. As shown earlier and by *Manoj* (2007), the daily equatorial enhancement of the field has its peak at 11 a.m. LT. However, figure 5.6(c) shows the peak amplitude to be around 2 p.m. LT in despite the Dst correction having already been done. This peak time corresponds to the initial phase of the storm, therefore a possible explanation for this shift of the peak time is the penetration of the polar electric field to the equator as previously suggested by other authors (*Nishida* 1968; *Kikuchi et al.* (1996, 2003, 2008)). The larger width of the EEJ observed during this time compared with that observed for the normal EEJ also indicates that the effects of such a penetration of the electric field occur broadly. In the region between t_1 and t_2, that is, the main phase of the storm, the depression of equatorial enhancement of the field can be seen at around 7 a.m. LT in figure 5.8(c), which indicates a westward current flow at that point. The possible explanation for this westward current is the disturbance dynamo (*Blanc and Richmond*, 1980) though the response in this case appears very quickly. Another possibility is just that the CEJ occurred during this period since the depression is only seen in the morning. Regardless, the analysis of atmospheric dynamics is necessary for further investigations. The EEJ current structure during this time is shown in figure 5.9, and it shows a very narrow westward-flowing current for all LTs around -15 degrees of latitude. This estimation was due to the abnormally small amplitude of the equatorial enhancement at NAZ, and may indicate that local electric current flows in a direction that reduces the field at that point. A unique LT variation of the equatorial enhancement variation can be seen in figure 5.10(c), which has double peaks at 9 a.m. and 3 p.m. LT. These double peaks may indicate that the variation was depressed between 9 a.m. and 3 p.m. LT because of disturbance dynamo, which originally peaks around noon. The LT distribution of the equatorial enhancement variation is different from that obtained by *Yamazaki and Kosch* (2014). They showed a negative value of the equatorial enhancement during the recovery phase of a geomagnetic storm. This is possibly due to the criteria of their timing being different in their study than that in this study since they statistically analyzed their data while only one case study was performed in this study. Although the contribution should be small, there is also the possibility of an overestimated Dst origin variation at PIU, which would result in a larger variation of the enhanced field.

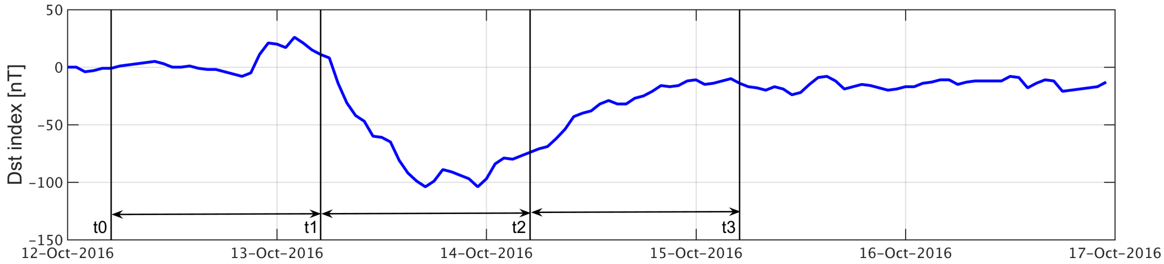

Figure 5.5 Time series of the Dst index between October 12 and October 17 in 2016, where t_0, t_1, t_2, and t_3 are defined by the date in Peru.

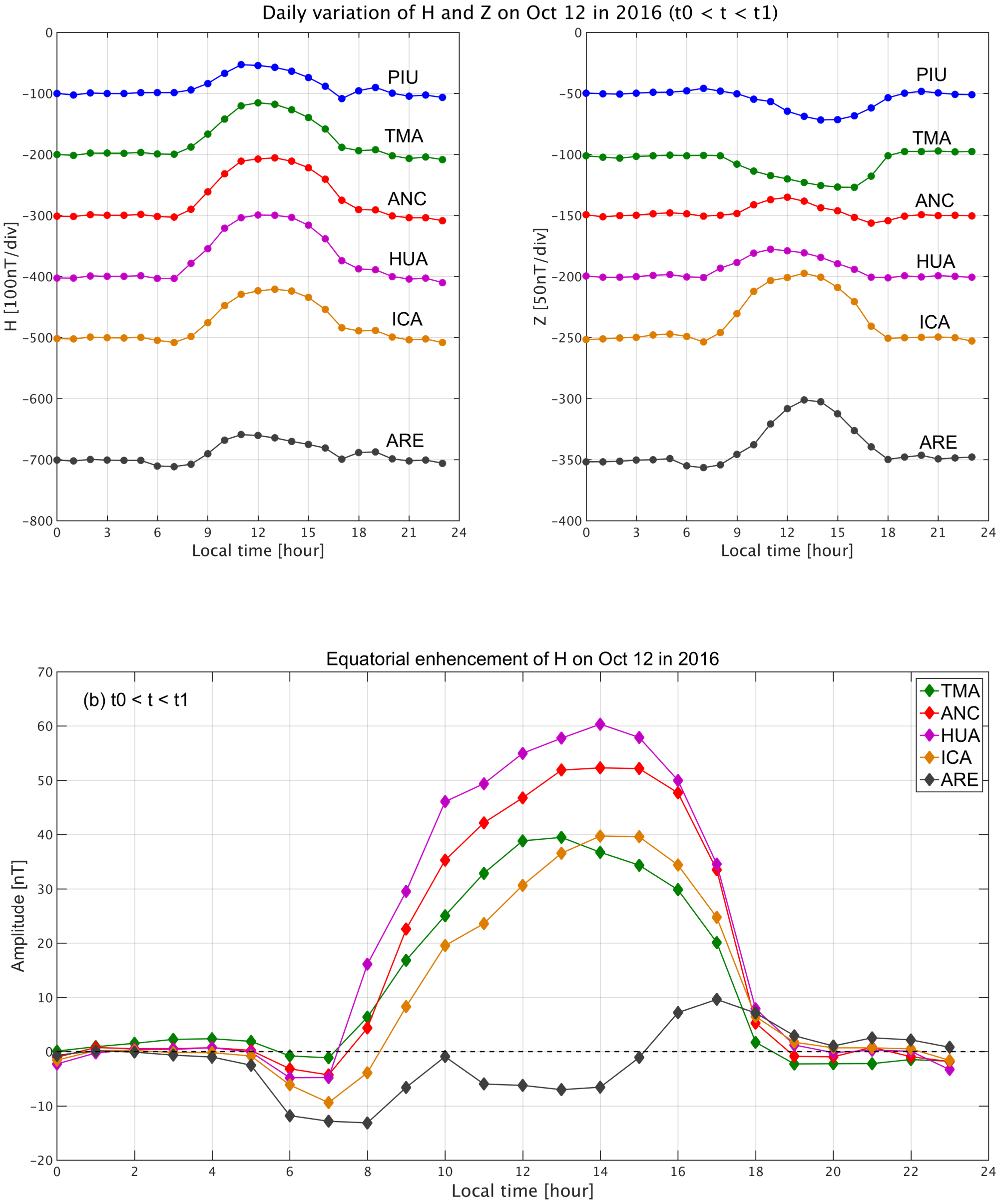

Figure 5.6 Same as those in figure 5.1 except that the data are for October 12, 2016 before the main phase of the geomagnetic storm

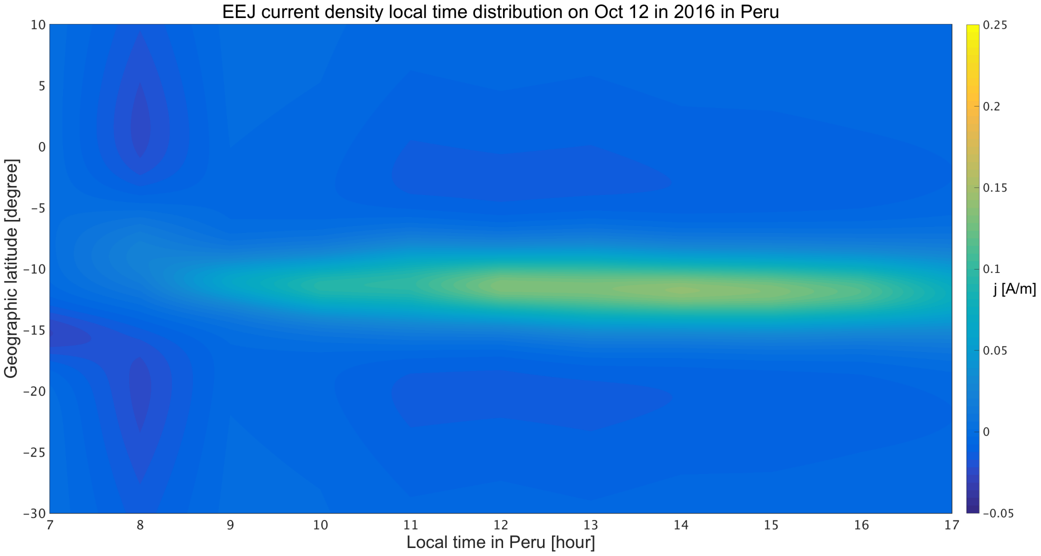

Figure 5.7 Same as in figure 5.2 but for the data from October 12, 2016

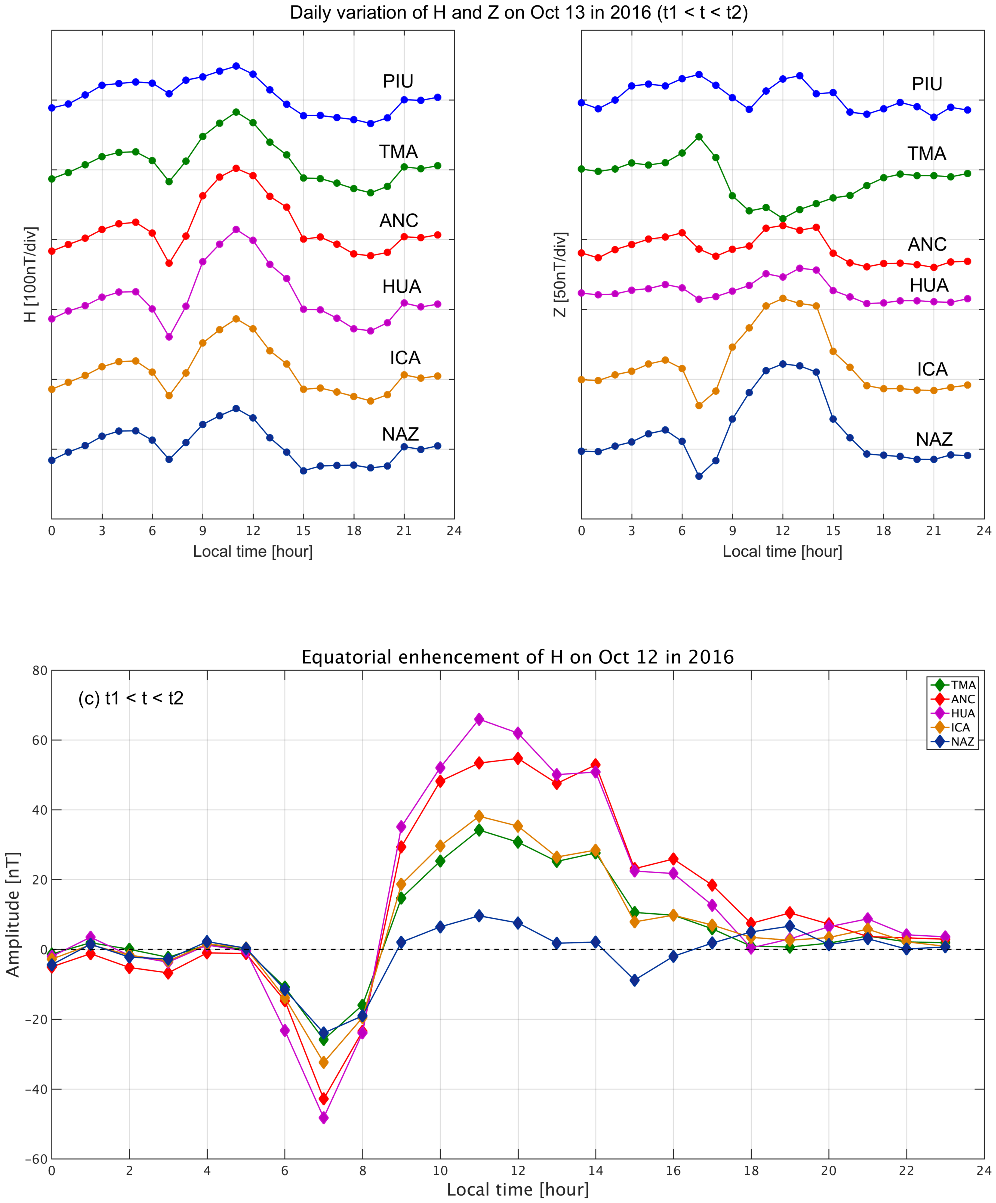

Figure 5.8 Same as those in figure 5.1 except that the data are from October 13, 2016 during the main phase of the geomagnetic storm

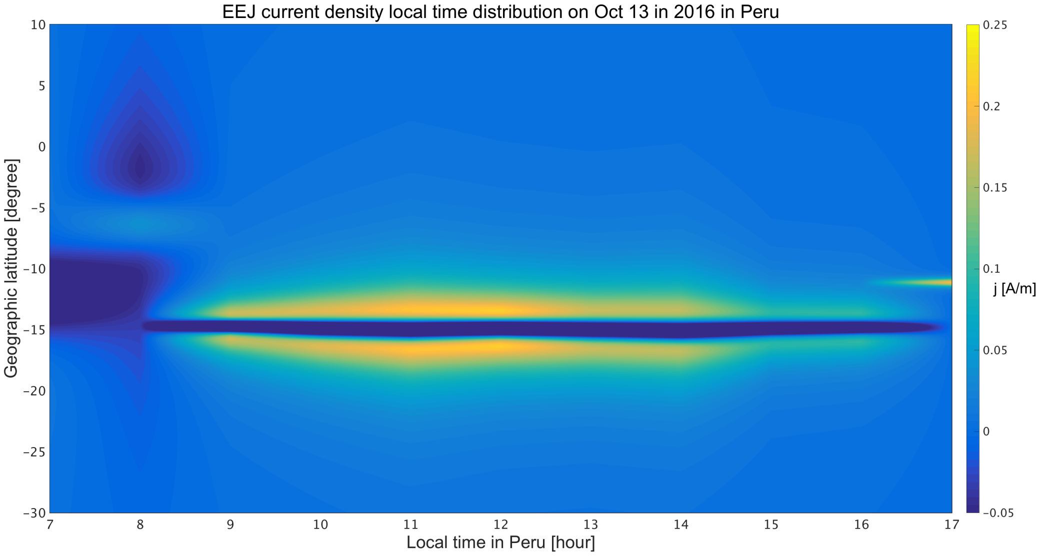

Figure 5.9 Same as in figure 5.2 but for the data from October 13, 2016

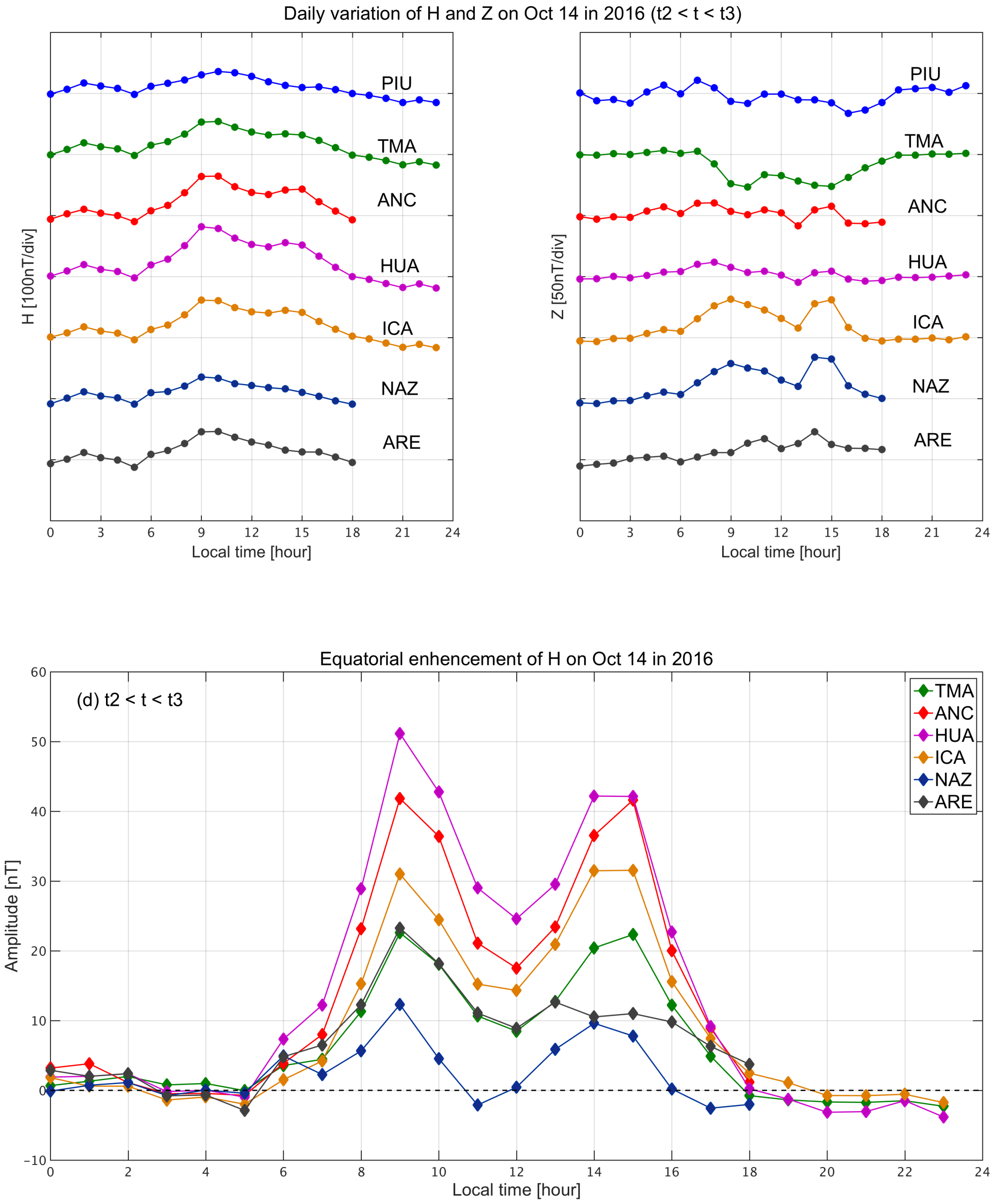

Figure 5.10 Same as those in figure 5.1 excepting that the data are from October 14, 2016 during the recovery phase of the geomagnetic storm

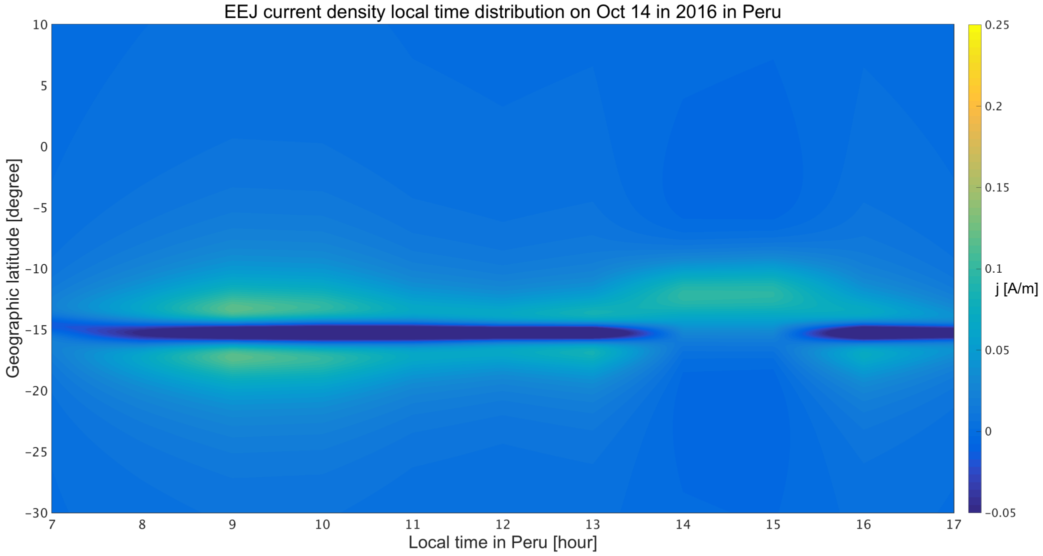

Figure 5.11 Same as figure 5.2 but for the data from October 14, 2016

6. Summary and Conclusions

In this study, the dense magnetometer array was developed in Peru to investigate the EEJ structural change continuously. In order to estimate the latitudinal profile of the EEJ current and the magnetic field produced by the EEJ, models were developed in this study, which could solve the problem in reverse, that is, the physical model of the EEJ current was set using some parameters and solved for its magnetic field on the ground to compare to an observed field. In addition, the modeled fields were compared with the Swarm-satellite magnetic data that were finely distributed in the observed latitudinal direction in order to evaluate the model. The results of the comparison are summarized as follows:

1. Good correspondences were observed between 9 a.m. and 11 a.m. LT.
2. Large discrepancies were observed at dawn and dusk due to the difficulties in the separation of the equatorial enhancement and the Sq variation.
3. The estimation of a larger or smaller amplitude of the current density compared to other values was possibly due to different assumed altitudes of the EEJ, where 110 km was adopted in this study.

Although the effect of number 3 above may produce ten percent of the differences in current density, it is difficult to estimate the altitude using only ground-based magnetometer readings. Therefore, an alternative method or observation is necessary to estimate the proper altitude of the EEJ.

In addition to the evaluation of the model, the long-term variations of the estimated EEJ structural parameters were investigated in order to confirm which parameters contribute to producing the long-term variations of the daily amplitude of the equatorial enhancement of the magnetic field. The results are summarized as follows:

1. The long-term variations of the field were well correlated with the peak amplitude of the EEJ current density, while other parameters such as the width of the EEJ and the position of the EEJ axis were not.
2. Correlations between the EEJ parameters and F10.7 were not found, and additionally, a correlation between the equatorial enhancement of the field and F10.7 was also not found. In other words, F10.7, one of the indexes used to determine the strength of the ionization, did not substantially affect the day-to-day variability of the EEJ structure including the current intensity.
3. Both the width and the position of the EEJ axis tended to move towards a certain value or become less dispersed when the equatorial enhancement of the field became larger. This was probably due to the extracted field including Sq variation for small fields.

In conclusion, the long-term variation of the equatorial enhancement of the daily variation was related to the EEJ current density. However, the correlations between the peak current density and F10.7 were not shown in this study. Therefore, other sources for the production of the long-term variation of the current density itself must be investigated.

As shown in Chapter 5, the features of the EEJ structure for different situations were investigated with some case studies. The results can be summarized as follows:

1. During a normal EEJ, the peak densities for the EEJ and its return current were seen at 11 a.m. and 1 p.m. LT, around -12 degrees of geographic latitude and ±7 degrees away from the EEJ axis. Moreover, the return current extended to nearer the dip equator after 1 p.m. LT.
2. During a morning CEJ, a smaller amplitude of the current density for the entire day could be seen, which was almost half the corresponding value for a normal EEJ day. Although there is day-to-day variability in the EEJ amplitude, it is probable that this smaller EEJ resulted from weakened eastward electric field by a westward electric field in the morning.
3. During the storm time EEJ, the enhanced current density during the initial phase and the main phase could be explained by a penetrating eastward electric field from the polar region. The negative or much smaller amplitude of the EEJ was probably due to the additional westward current caused by disturbance dynamo. This effect seemed to be largest around the NAZ station.

Regarding future work using this model, the detailed latitudinal structure of some disturbance phenomena such as DP2 can be revealed. Moreover, it was shown that combining the ground magnetic data and the LEO magnetic data is a great tool to estimate the altitude of the current or the local current on the ground, hence, more realistic current structures can be derived. Though the dense magnetometer array in Peru consists of seven magnetometer stations, more datasets are desirable especially around the region in which the return current flows, which is approximately ±5° of latitude away from dip equator, to acquire a more accurate EEJ structure. Additionally, statistical analysis of the LT structure of the EEJ is also recommended in order to investigate the general features of the EEJ and the relationship between the amplitude of the equatorial enhancement field and the current structure.

List of references

Alken, P., and Maus, S. (2007), Spatio–temporal characterization of the equatorial electrojet from CHAMP, Ørsted, and SAC‐C satellite magnetic measurements, J. Geophys. Res., 112, A09305, doi:10.1029/2007JA012524.

Bartles, J., and Johnston, H. F., (1940b), Geomagnetic tides in horizontal intensity at Huancayo - I, J. Geophys. Res., 45, 269-308.

Bartles, J., and Johnston, H. F., (1940a), Geomagnetic tides in horizontal intensity at Huancayo - II, J. Geophys. Res., 45, 485-592.

Blanc, M., and A. D. Richmond (1980), The ionospheric disturbance dynamo, J. Geophys. Res., 85(A4), 1669–1686, doi:10.1029/JA085iA04p01669.

Burrage, M. D., M. E. Hagan, W. R. Skinner, D. L. Wu, and P. B. Hays (1995), Long‐term variability in the solar diurnal tide observed by HRDI and simulated by the GSWM, Geophys. Res. Lett., 22, 2641–2644.

Cain, J. C., and Sweeney, R. E., (1973), The POGO data, Journal of Atmospheric and Terrestrial Physics, 35, 1231-1247.

Chapman, S. (1951), The equatorial electrojet as detected from the abnormal electric current distributions above Huancayo, Peru, and elsewhere, Arch. Meteorol. Geophys. Bioclimatol, A4, 368–390.

Davis,T.N. K., Burrows, J.D. Stolarik (1967), A latitude survey of the equatorial electrojet with rocket-borne magnetometers. J. Geophys. Res. 72, 1845–1861.

Deminov, M. G., N. A. Kochenova, and Y. S. Sitnov (1988), Longitudinal variations of the electric field in the dayside equatorial ionosphere, Geomagnetism and Aeronomy, 28, 57-60.

Fambitakoye, and P. N. Mayaud (1976), Equatorial electrojet and regular daily variation SR-1. A determination of the equatorial electrojet parameters, Journal of Atmospheric and Terrestrial Physics, 38, 1-17.

Fejer, B.G., Scherliess , L. (1995), Time dependent response of equatorial ionospheric electric fields to magnetospheric disturbances. Geophys. Res. Lett. 22(7), 851–854. doi:10.1029/95GL00390.

Fejer, B.G., Scherliess, L., (1997). Empirical models of storm time equatorial zonal electric fields. J. Geophys. Res. 102, 24047–24056.

Forbes, J. M. (1981), The equatorial electrojet, Reviews of Geophysics and Space Physics, 19, 469–504.

Fujimoto, A., Uozumi, T., Abe, S., Matsushita, H., Imajo, S., Ishitsuka, J. K. and Yoshikawa, A. (2016), Long-term EEJ variations by using the improved EE-index, Sun and Geosphere, Vol.11, Issue 1.

Gonzales, C. A., Kelley, M. C., Fejer, B. G., Vickrey, J. F., Woodman, R. F. (1979), Equatorial electric fields during magnetically disturbed conditions, 2, Implications of Simultaneous Auroral and Equatorial Measurements, J. Geophys. Res., 84, 5803–5812.

Motokazu HIRONO (1950a), On the Influence of the Hall Current to the Electrical Conductivity of the Ionosphere. I, Journal of geomagnetism and geoelectricity, Volume 2, Issue 1, Pages 1-8.

Motokazu HIRONO (1950b), On the Influence of the Hall Current to the Electrical Conductivity of the Ionosphere. II, Journal of geomagnetism and geoelectricity, Volume 2, Issue 4, Pages 113-120.

Motokazu HIRONO (1952), A Theory of Diurnal Magnetic Variations in Equatorial Regions and Conductivity of the Ionosphere E Region, Journal of geomagnetism and geoelectricity, Volume 4, Issue 1, Pages 7-21.

Motokazu HIRONO (1953), A Theory of Diurnal Magnetic Variations in Equatorial Regions and Conductivity of the Ionosphere E Region, Part II, Journal of geomagnetism and geoelectricity, Volume 5, Issue 1-2, Pages 22-38.

Hamid, N.S.A., Liu, H., Uozumi T. and Yumoto, K. (2013), Equatorial electrojet dependence on solar activity, Nankyoku Shiryo (Antarctic Record), Vol. 57, No. 3, 329-337.

Huang, C., Liu, D. D. and Wang, J. S. (2009), Forecast daily indices of solar activity, F10.7, using support vector regression method, Research in Astron. Astrophys, 9(6), 694–702.

Hutton, R. (1967), Sq currents in the American equatorial zone during the IGY—I Seasonal effects, Journal of Atmospheric and Terrestrial Physics, 29, 1411–1427.

Jadhav, G., Rajaram, M. and Rajaram, R. (2002), A detailed study of equatorial electrojet phenomenon using Ørsted satellite observations. J. Geophys. Res. 107(A8), 1175. doi:10.1029/2001JA000183.

Kelley, M. C., Baker, K. D. and Ulwick, J. C. (1979), AC electric field measurements in the equatorial electrojet (abstract), EOS Trans. AGU. 60, 335.

Kerridge, D. (2001), INTERMAGNET: Worldwide near-real-time geomagnetic observatory data, in Space Weather Workshop: Looking Towards a European Space Weather, edited, Eur. Space Res. and Technol. Cent., Noordwijk, Netherlands.

Kikuchi, T., Lühr, H., Kitamura, T., Saka, O., Schlegel, K. (1996), Direct penetration of the polar electric field to the equator during a DP 2 event as detected by the auroral and equatorial magnetometer chains and the EISCAT radar
, Journal of Geophysical Research, 101, A8.

Kikuchi, T., Hashimoto, K. K., Kitamura, T.-I., Tachihara, H. and Fejer, B. (2003), Equatorial counterelectrojets during substorms, J. Geophys. Res., 108(A11), 1406, doi:10.1029/2003JA009915.

Kikuchi, T., Hashimoto, K. K. and Nozaki, K. (2008), Penetration of magnetospheric electric fields to the equator during a geomagnetic storm, J. Geophys. Res., 113, A06214, doi:10.1029/2007JA012628.

Liu, L., Wan, W., Ning, B., Pirog, O. M. and Kurkin, V. I. (2006), Solar activity variations of the ionospheric peak electrondensity, J. Geophys. Res., 111, A08304, doi:10.1029/2006JA011598.

Le Mouel, J. L., Shebalin, P. and Chulliat, A. (2006), The field of the equatorial electrojet from CHAMP data, Ann. Geophys., 24, 515–527.

Lühr, H., Maus, S. and Rother, M. (2004), Noon-time equatorial electrojet: Its spatial features as determined by the CHAMP satellite. J. Geophys. Res. 109, A01306. doi:10.1029/2002JA009656.

Mann, R. J., and Schlapp, D. M. (1988), The equatorial electrojet and the day-today variability of Sq, Journal of Atmospheric and Terrestrial Physics, 50(1), 57-62.

Manoj, C., Lühr, H., Maus, S. and Nagarajan, N. (2006), Evidence for short spatial correlation lengths of the noontime equatorial electrojet inferred from a comparison of satellite and ground magnetic data, Journal of Geophysical Research, 111, A11312, doi:10.1029/2006JA011855.

Maynard, N.C., and Cahill, L. J. Jr. (1965), Measurement of the equatorial electrojet over India, Journal of Geophysical Research, 70, 5923-5936.

Maynard, N.C. (1967), Measurements of ionospheric currents off the coast of Peru. J. Geophys. Res. 72(7), 1863–1875. doi:10.1029/JZ072i007p01863.

Nishida, A. and Jacobs, J. A. (1962), World-Wide Changes in the Geomagnetic Field, Journal of Geophysical Research, Vol 67, No. 2.

Nishida, A. (1968), Coherence of DP 2 fluctuations with interplanetary magnetic field variations, J. Geophys. Res., 73, 5549–5559.

Onwumechili, C. A. (1965a), A three dimensional model of density distribution of ionospheric current causing part of quiet day geomagnetic variations, Proc. Second International Symposium on Equatorial Aeronomy, Ed. F. de Mendonca, Brazilian Space Commission, Sao Paulo, 384-386.

Onwumechili, C. A. (1965b), The magnetic field of a current model for part of geomagnetic

Sq variations, Proc. Second International Symposium on Equatorial Aeronomy, Ed. F. de Mendonca, Brazilian Space Commission, Sao Paulo, 387-390.

Onwumechili, C. A. (1967), Geomagnetic variations in the equatorial zone; In: Physics of geomagnetic Phenomena, Vol. 1 Chap. III-2, 425-507, Eds. Matsushita, S. and Campbell, W.H., Academic Press, New York.

Onwumechili, C. A. (1992a), A study of rocket measurement of ionospheric currents.-IV. Ionospheric currents in the transition zone and the overview of the study, Geophysical Journal International, 108, 660-672.

Onwumechili, C. A. (1992b), Study of the Return Current of the Equatorial Electrojet, Journal of Geomagnetism and Geoelectricity, 44, 1-42.

Onwumechili, C. A. (1997), The Equatorial Electrojet, 627 pp., Gordon and Breach Science Publishers, Amsterdam, The Netherlands.

Onwumechili, C. A., and Agu, C.E. (1980), General features of the magnetic field of the equatorial electrojet measured by POGO satellites, Planet Space Sci., 28, 1125-1130.

Onwumechili, C. A., and Agu, C.E. (1981a), The relationship between the current and the width of the equatorial electrojet, Journal of Atmospheric and Terrestrial Physics, 43, 573-578.

Onwumechili, C. A., and Agu, C.E. (1981b), Longitudinal variations of equatorial electrojet parameters derived from POGO Satellite observations, Planet Space Sci., 29, 627-634.

Onwumechili, C. A., and Ezema, P. O. (1992), Latitudinal and vertical parameters of the equatorial electrojet from an autonomous data set, Journal of Atmospheric and Terrestrial Physics, 54(11), 1535-1544. 70.

Scherliess, L., and Fejer, B. G. (1997), Storm time dependence of equatorial disturbance dynamo zonal electric fields, J. Geophys. Res., 102(A11), 24,037–24,046, doi:10.1029/97JA02165.

Shuman, B. M. (1970), Rocket measurement of the equatorial electrojet, Journal of Geophysical Research, 75, 3889-3901.

Stening, R. J. (1995), What drives the equatorial electrojet?, Journal of Atmospheric and Terrestrial Physics, 57, 1117–1128.

SUZUKI, A. and MAEDA, H. (1968), A Simple Model of the Equatorial Electrojet, Journal of geomagnetism and geoelectricity, Volume 20, Issue 1, Pages 51-53.

SUZUKI, A. (1973), A New Analysis of the Geomagnetic Sq Field, Journal of geomagnetism and geoelectricity, Volume 25, Issue 3, Pages 259-280.

Untiedt, J. (1967), A model of the equatorial electrojet involving meridional currents. J. Geophys. Res. 72, 5799–5810.

Uozumi, T., et al. (2008), A new index to monitor temporal and long-term variations of the equatorial electrojet by MAGDAS/CPMN real-time data: EEIndex, Earth Planets Space, 60, 85–790.

Wei, Y., Wan, W., Zhao, B., Hong, M. Ridley, A., Ren, Z. Fraenz M., Dubinin, E. and He, M. (2012), Solar wind density controlling penetration electric field at the equatorial ionosphere during a saturation of cross polar cap potential, J. Geophys. Res., 117, A09308, doi:10.1029/2012JA017597.

Yamazaki, Y., Yumoto, K., Uozumi, T., Abe, S., Cardinal, M. G., McNamara D., Marshall,R., Shevtsov, B. M. and Solovyev, S. I. (2010), Reexamination of the Sq-EEJ relationship based on extended magnetometer networks in the east Asian region, Journal of Geophysical Research, 115, A09319, doi:10.1029/2010JA015339.

Yamazaki, Y., and Kosch, M. J. (2015), The equatorial electrojet during geomagnetic storms and substorms, J. Geophys. Res. Space Physics, 120, 2276–2287, doi:10.1002/2014JA020773.

Yumoto, K., and the MAGDAS Group (2006), MAGDAS project and its application for space weather, in Solar Influence on the Heliosphere and Earth's Environment:

Recent Progress and Prospects, edited by N. Gopalswamy and A. Bhattacharya, pp. 399–405, Quest Publications, Wheaton.

Yumoto, K., and the MAGDAS Group (2007), Space weather activities at SERC for IHY: MAGDAS, Bull. Astr. Soc. India, 35, 511–522.